metals

MDPI

Article

Additive Manufacturing of Tungsten Carbide (WC)-Based Cemented Carbides and Niobium Carbide (NbC)-Based Cermets with High Binder Content via Laser Powder Bed Fusion

Fabio Miranda [1,2,*], Marcelo Otavio dos Santos [3,4], Rodrigo Condotta [3], Nathalia Marina Gonçalves Pereira [3], Daniel Rodrigues [2], Suzilene Real Janasi [2], Fernando dos Santos Ortega [5], Marcello Vertamatti Mergulhão [6], Rodrigo Santiago Coelho [6], René Ramos de Oliveira [7], Luis Gallego Martinez [7] and Gilmar Ferreira Batalha [1]

[1] Polytechnic School, University of São Paulo, EPUSP–PMR, São Paulo 05508-220, São Paulo, Brazil; gfbatalh@usp.br
[2] BRATS Sintered Filters and Special Powder Composites, Cajamar 07750-000, São Paulo, Brazil; daniel@brats.com.br (D.R.); srjanasi@yahoo.com.br (S.R.J.)
[3] Chemical Engineering Department, University Center FEI, São Bernardo do Campo 09850-901, São Paulo, Brazil; marcelo.santos@maua.br (M.O.d.S.); rcondotta@fei.edu.br (R.C.); unienpereira@fei.edu.br (N.M.G.P.)
[4] Mauá Institute of Technology, University Centre, São Caetano do Sul 09580-900, São Paulo, Brazil
[5] Research and Development Institute, University of Vale do Paraíba, São José dos Campos 12244-000, São Paulo, Brazil; ortega@univap.br
[6] SENAI CIMATEC—Institute of Innovation for Forming & Joining of Materials, Salvador 41650-010, Bahia, Brazil; marcello.mergulhao@fieb.org.br (M.V.M.); rodrigo.coelho@fieb.org.br (R.S.C.)
[7] IPEN, Institute of Energy and Nuclear Research, São Paulo 05508-000, São Paulo, Brazil; reneoliveira.ipen@gmail.com (R.R.d.O.); lgallego@ipen.br (L.G.M.)
* Correspondence: fabio.miranda@usp.br

Citation: Miranda, F.; dos Santos, M.O.; Condotta, R.; Pereira, N.M.G.; Rodrigues, D.; Janasi, S.R.; Ortega, F.d.S.; Mergulhão, M.V.; Coelho, R.S.; de Oliveira, R.R.; et al. Additive Manufacturing of Tungsten Carbide (WC)-Based Cemented Carbides and Niobium Carbide (NbC)-Based Cermets with High Binder Content via Laser Powder Bed Fusion. *Metals* **2024**, *14*, 1333. https://doi.org/10.3390/met14121333

Academic Editors: Costanzo Bellini and Golden Kumar

Received: 10 October 2024
Revised: 15 November 2024
Accepted: 18 November 2024
Published: 25 November 2024

Abstract: The additive manufacturing technique performed via laser powder bed fusion has matured as a technology for manufacturing cemented carbide parts. The parts are built by additive consolidation of thin layers of a WC and Co mixture using a laser, depending on the power and scanning speed, making it possible to create small, complex parts with different geometries. NbC-based cermets, as the main phase, can replace WC-based cemented carbides for some applications. Issues related to the high costs and dependence on imports have made WC and Co powders emerge as critical raw materials. Furthermore, avoiding manufacturing workers' health problems and occupational diseases is a positive advantage of replacing WC with NbC and alternative binder phases. This work used WC and NbC as the main carbides and three binders: 100% Ni, 100% Co, and 50Ni/50Co wt.%. For the flowability and spreadability of the powders of WC- and NbC-based alloy mixtures in the powder bed with high cohesiveness, it was necessary to build a vibrating container with a pneumatic turbine ranging from 460 to 520 Hz. Concurrently, compaction was promoted by a compacting system. The thin deposition layers of the mixtures were applied uniformly and were well distributed in the powder bed to minimize the defects and cracks during the direct sintering of the samples. The parameters of the L-PBF process varied, with laser scanning speeds from 25 to 125 mm.s^{-1} and laser power from 50 to 125 W. Microstructural aspects and the properties obtained are presented and discussed, seeking to establish the relationships between the L-PBF process variables and compare them with the liquid phase sintering technique.

Keywords: L-PBF; WC-based cemented carbides; NbC-based cermets; alternative binder phases; microstructural characterization; properties

1. Introduction

Cemented carbides are considered metal–ceramic materials and are processed by the powder metallurgy route, containing traditional elements such as tungsten carbides (WCs) and cobalt (Co). Alternative binder phases such as nickel (Ni) or combined (Co, Ni) are used [1]. The most commonly used cemented carbide alloy in the metalworking sector is based on WC-Co [2], mainly for machining, mining, cold-forming, and mechanical-forming processes, among other applications [3]. There are considerable efforts to develop new classes of cemented carbides, or those with alternative compositions, to improve these products' microstructure, mechanical properties, and performance. This quest to replace the WC-Co alloy is related to patent restrictions and the scarcity of Co ore, which have led Co and W ores to reach increasingly higher prices since the early 21st century [4]. Due to its worldwide consumption for battery manufacturing, Co is in short supply and, consequently, the commercial price is higher. Another important point is that Co in dust form, when released in the workplace, results in occupational diseases. Inhalable Co is classified as A3 (confirmed animal carcinogen with unknown relevance to humans) by the American Conference on Governmental Industrial Hygiene (ACGIH) and Ni is classified as A5 (not suspected as a human carcinogen). In 2016, the ACGIH made available specific data for cemented carbides (WC-Co), classified as A2 (suspected human carcinogen). Replacing Co with Ni, entirely or in part, with alternative binder phases (Co, Ni) is a great advantage, minimizing the health risks to workers during production [5,6]. Co has been classified as a critical raw material and global demand is expected to quadruple in the next four decades due to the high demand forecast [7]. Replacing Co with Ni may be beneficial from an occupational hygiene and cost perspective.

NbC-based cermets with alternative binder phases (NbC-Ni) have emerged to minimize the consumption of WC and Co and are manufactured by the conventional powder metallurgy route [8,9]. Their applications are focused on cutting tools for machining subject to wear resistance at high temperatures. In addition, they have greater corrosion resistance than Co [10]. They require high resistance to hot fracture and thermomechanical plastic deformation to withstand severe conditions, such as cold and hot rolling, extrusion and stamping [11]. In addition, they are resistant to wear and corrosion, combine at high temperatures and compete with combined WC-based cemented carbides (WC-Co) with small amounts of Cr_3C_2 and (Ti, Mo) C [12].

There are numerous scientific studies on adding small amounts of NbC to conventional WC-Co alloys to reinforce the binder phase [2] and as an inhibitor of abnormal WC grain growth [13]. NbC-based cermets have not been explored as the main phase [8,13,14]. The total replacement of WC by NbC for hard metal alloys was a difficult task. The raw material was very expensive and only available in small quantities due to there being few manufacturers or import restrictions [15]. Currently, rolling rolls, guide rolls, and rollers, among other products applied in the steel industry, are manufactured based on NbC-Ni cermets. The application of this class is well defined. The manufacture of cermets based on NbC-20Ni was a great challenge, requiring coarse NbC grains, hardness and microstructures equivalent to WC-Co alloys [16]. Brazil has the world's largest niobium reserves, making the study of new NbC applications a strategic research area [2,4].

Laser powder bed fusion (L-PBF) is a promising alternative for producing refractory alloys using computer-controlled layer-by-layer deposition [17], having as an advantage the ability to manufacture W-based alloy components with complex and complicated shapes and small dimensions, which cannot be easily manufactured by traditional methods, such as casting, forging machining, and conventional powder metallurgy [18,19]. Several industrial sectors have been using this technique to reduce production costs (eliminating inputs and manufacturing steps), mainly to manufacture high-value-added and low-volume mechanical components. Many researchers have highlighted the difficulties in manufacturing parts with tungsten-based alloys, as it involves high temperatures, rapid melting and localized solidification, mainly resulting in cracks [20].

Compared to the centuries-old conventional powder metallurgy technique, L-PBF has been identified as the best technology for manufacturing complex-shaped cemented carbide products [21]. The great challenge is to obtain products with high density, with an almost total absence of porosity and cracks, with a homogeneous, refined and as uniform as possible microstructure, and with good mechanical properties; and, such as the hardness and transverse rupture stress (TRS), equivalent to products from the conventional route [15].

This work aimed to compare conventional powder metallurgy (PM), via liquid phase sintering (LPS), with additive manufacturing (AM), via L-PBF (laser powder bed fusion), considering WC- and NbC-based cemented carbides with binders such as Co, Ni and Co and Ni mixtures. The great challenge was to improve the flowability to obtain a bed as homogeneous as possible, so, additionally, a vibrating container was used to spread the powder, trying to obtain a uniform layer. Conventional samples were produced by pressing and high-temperature vacuum sintering. For AM, the laser power versus speed was investigated. Analyses of the porosities, microstructures, hardness, phase analysis, and residual thermal stresses were evaluated to discuss the potential of L-PBF.

2. Materials and Methods

The conventional route cemented carbide samples were prepared (Table 1) with the following compositions (Table 2) in wt.%: (I) WC-30Co, (II) WC-30Ni, (III) WC-30(Co, Ni), (IV) NbC-30Co, (V) NbC-30Ni and (VI) NbC-30(Co, Ni). High-purity commercial Co, Ni, WC, and NbC powders were used, with the following average particle sizes: 2.0, 4.8, 1.5, and 1 µm. The refractory and metallic powders, as shown in Figure 1, were mixed and homogenized using a conventional high shear rate mixer for 2 h, using isopropyl alcohol to promote a homogeneous suspension, avoiding deformation of the metallic particles, Co and Ni. After the mixing step, isopropyl alcohol was removed by conventional drying in an oven at 200 °C for 2 h. The raw materials NbC, WC, Ni, and Co, as shown in Table 1, were evaluated for the particle size distribution using a particle size analyzer for non-spherical particles, Microtrac S3550 (Microtrac Retsch GmbH, Haan, Germany), with laser diffraction with 25 nm precision, which measures particle sizes from 0.02 to 2800 µm. To analyze the actual densities of the powders, an automatic helium pycnometer, AccuPyc II 1350 (Micromeritics Instrument Corporation, Norcross, GA, USA), was used to measure the volume and density of the solids, and the Gemini II N_2 physisorption equipment (Micromeritics Instrument Corporation, Norcross, GA, USA) was used to obtain the surface area and average pore diameter. In Table 1, the theoretical densities of the mixtures are considered, along with the content of 6.14 wt.% carbon, and compared with the actual densities obtained in the pycnometer test, the real densities.

Table 1. Properties of refractory ceramic and metallic powders.

Powders	Theoretical Density (g.cm^{-3})	Average Grain Size FSSS (µm)	Purity (wt.%)	Carbon (wt.%)	Bulk Density (g.cm^{-3})	Origin
WC	15.63	1.5	99.53	5.8	4.0	Buffalo Tungsten Inc. (Depew, NY, USA)
NbC	7.65	<1.0	99.65	7.8	3.0	F&X Electro-Materials Limited (Jiangmen, China)
Co	8.91	2.2	99.87	<0.03	1.2	Nanjing Hanrui Cobalt Co. (Nanjing, China)
Ni	8.91	4.8	99.85	-	2.5	CVMR Corporation (Toronto, ON, Canada)

Information obtained from manufacturers' quality certificates.

Table 2. Weight balance for the prepared alloys.

Alloy	Powders	Weight Balance (%)				Theoretical Density (g.cm^{-3})	Pycnometric Density (g.cm^{-3})
		WC	NbC	Co	Ni		
(I)	WC-30Co	70.0		30.0	0.0	12.74	12.38
(II)	WC-30Ni	70.0		0.0	30.0	12.75	12.71
(III)	WC-30(Co, Ni)	70.0		15.0	15.0	12.75	12.54
(IV)	NbC-30Co	3.0	67.0	30.0	0.0	8.03	7.86
(V)	NbC-30Ni	3.0	67.0	0.0	30.0	8.05	7.99
(VI)	NbC-30(Co, Ni)	3.0	67.0	15.0	15.0	8.04	7.93

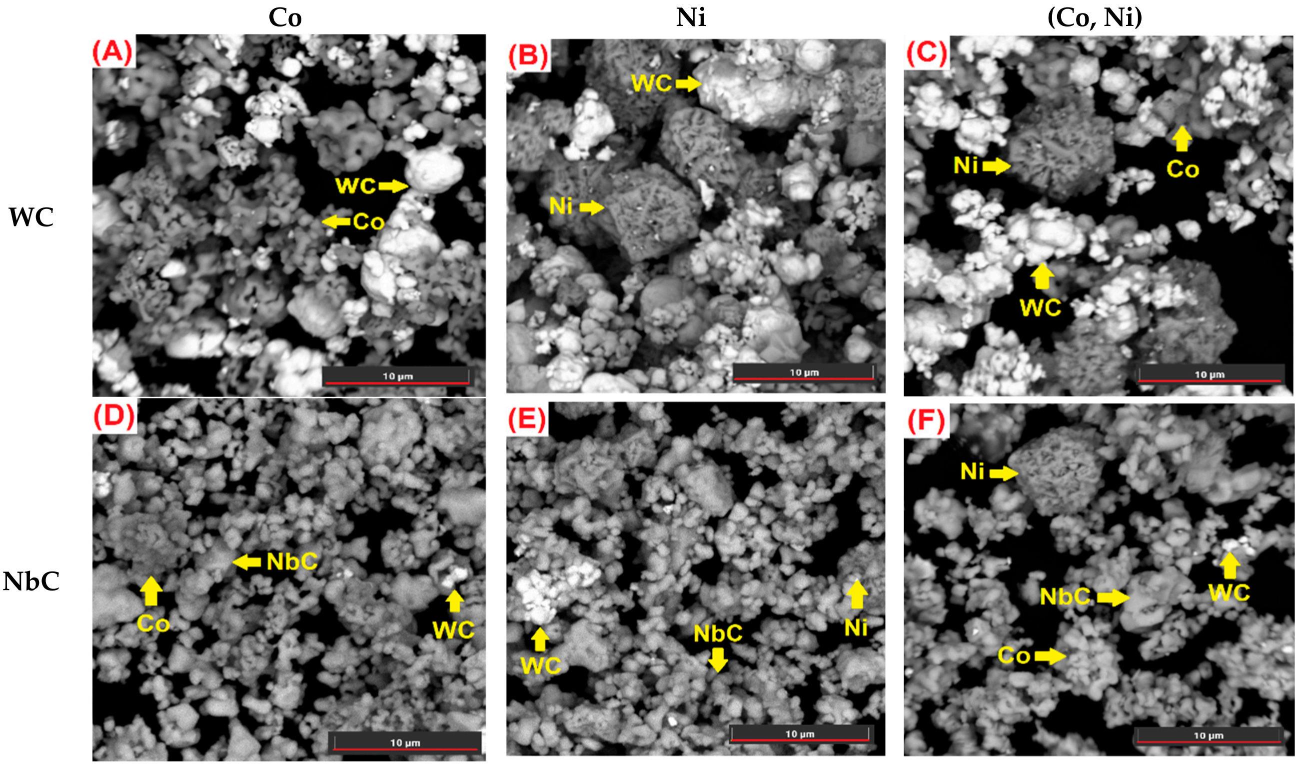

Figure 1. BSE-SEM images of the mixtures: (**A**) WC-30 Co, (**B**) WC-30 Ni, (**C**) WC-30 (Co, Ni), (**D**) NbC-30 Co, (**E**) NbC-30 Ni and (**F**) NbC-30 (Co, Ni).

Figure 1A–F show the BSE-SEM images of the WC- and NbC-based mixtures. In Figure 1C,F, showing the identification of the Ni and Co powders, the particle shapes are different. Ni has a dendritic and porous shape with dimensions smaller than 10 µm. Electrolytic Co presents irregular shapes and aggregates with sizes smaller than 1 µm (submicron). For the refractory powders, WC presents particles of higher apparent density in an irregular shape (non-spherical), with an average grain size smaller than 10 µm. For NbC, as shown in Table 1, it presents a lower apparent density when compared to the density of WC. In Figure 1D–F, the particles are observed to be irregular and polygonal, with an average size of less than 1 µm.

The flowability of these mixed powders in the vibrating pneumatic device (Figure 2) is not an inherent property, which depends not only on the physical properties but also on the stress state, the equipment used, and the handling method, since these are conventional metallurgy powders, with difficulty flowing or cohesive. To analyze the granulometric distribution of the mixtures according to Table 2, a sieve shaker was used—LGI Scientific, model LGI-VW-SSO (Laborglas, São Paulo, Brazil) with standardized sieves, capacity of 6 sieves at most: #100 (150 µm), #200 (75 µm), #325 (44 µm), #400 (37 µm), #500 (25 µm) and #600 (15 µm) mesh Tyler, in decreasing order of openings.

A pneumatic device with a vibrating container was developed, coupled with a metallic roller, as shown in Figure 2A–D, whose rotation speed was controlled independently of its displacement speed. Compaction was performed with a polished stainless steel metal roller inside the sintering chamber in the powder bed, as in Figure 2C [22]. Compacting thin layers with a compactor roller is interesting for extra-fine powder composites for applications focused on only AM in metals [23]. In this compaction operation with the metal roller, the powder mixtures needed to flow through the lower part of the pneumatic container and be concurrently spread and compacted. For this, it was necessary to select and determine a sieve, or stainless-steel mesh, to control the deposition flow of powders from the prepared mixtures. For this device, as shown in Figure 2C, it was impossible to evaluate the rheological behavior of the powder composites to obtain the flow energy of the samples to quantify the resistance to flow for a better understanding of the behavior of the mixtures in the powder bed, as in Figure 2D.

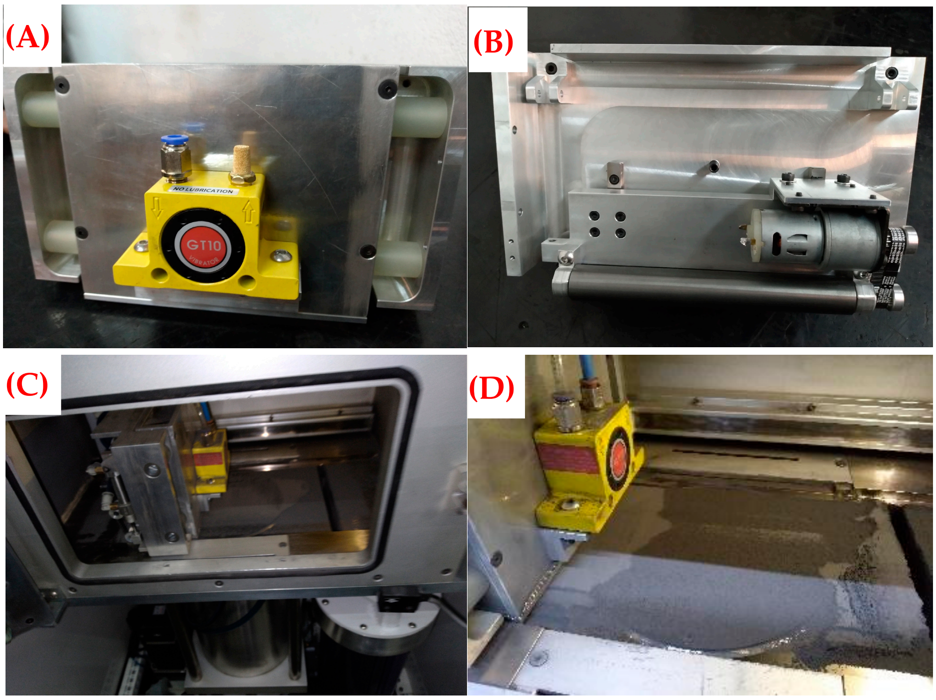

Figure 2. Pneumatic vibrating device coupled to a metal compactor roller: (**A**) front view; (**B**) rear view; (**C**) sintering chamber and pneumatic vibrating device installed inside the sintering chamber; and (**D**) flowability and spreadability test of powder mixtures in the powder bed.

The layer on the powder bed was created by a vibrating device (capacity 1500 g) with a rubber scraper ruler and a compactor roller at the bottom of the device, as in Figure 2B. The speed of the device and the rotation of the roller were controlled. The powder bed area was vast (about 630 cm^2), and the compaction force was applied by a 2 kgf (19.613 N) roller. The powder drained from the device through a #35 mesh/Tyler sieve [22]. The translational movement of the device simultaneously spread and compacted the powder, generating layers in the powder bed of 30 to 100 µm. As depicted in Figure 2C, the sintering chamber presented a controlled atmosphere of high-purity argon (>99.99%), with a continuous flow rate of 0.3 L.min^{-1}. Several operational parameters associated with this new compaction strategy can be adjusted and controlled to modify the compacted layer in the dust bed; the effect of the roller compaction force on the properties of the powdered composites is one of the main variables [23].

To better understand the rheological behavior of these composites, an FT-4 Powder Rheometer® was used. Results were obtained using a patented measuring principle that evaluated the resistance to movement of a specially shaped twisted blade that goes through a precise volume of sample along a prescribed path. The required torque and force were recorded and converted into flow energy [24]. Repeated testing of a single sample (with intermediate reconditioning) can be used to evaluate the physical stability of a powder (described by the Stability Index—SI). Changes in the blade speed can be used to determine how the powder responds to being made to flow at different rates (described by the Flow Rate Index—FRI) [25]. The granules' rheological properties can be obtained in the Powder Rheometer® and are influenced by the processing parameters: compressibility, bulk/tapped density, aeration, the primary energy of flow, and shear [24,26]. However, it is difficult to observe this L-PBF process to obtain critical parameters that demonstrate a direct influence on the performance of the compacted layer in the powder bed [22]. For the L-PBF process parameters, as in Figure 3A, the tracks were created using laser powers

(P_L) as a function of the scanning speed (V_s). According to the scanning system of the OmniSinter-160 equipment (Omnitek Tecnologia, São Paulo, Brazil), P_L = 457 W (100%), the scanning speed was varied from 25–125 mm.s^{-1}, changing 50–125 W while maintaining the Hs = 80 µm of the Iz = 30 µm, laser focus diameter 140 µm. The volumetric energy density (VED) applied to the WC- and NbC-based cemented carbides can be calculated by Equation (1) [27,28], where the VED (J.mm^{-3}) is equivalent to the VED that relates the power (P_L) with the scanning speed (v_S), track distance (h_S) and layer thickness (I_Z).

$$\mathrm{VED} = \frac{P_L}{v_S \cdot h_S \cdot I_Z} \quad (1)$$

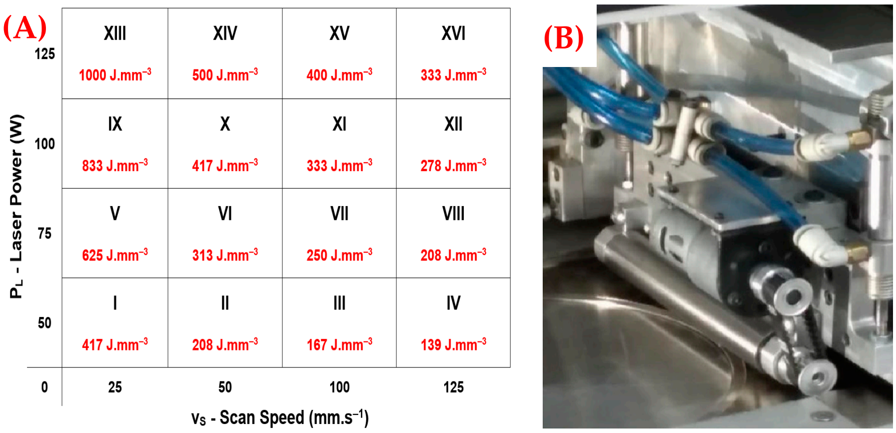

P_L (W) \ v_S (mm.s^{-1})	25	50	100	125
125	XIII 1000 J.mm^{-3}	XIV 500 J.mm^{-3}	XV 400 J.mm^{-3}	XVI 333 J.mm^{-3}
100	IX 833 J.mm^{-3}	X 417 J.mm^{-3}	XI 333 J.mm^{-3}	XII 278 J.mm^{-3}
75	V 625 J.mm^{-3}	VI 313 J.mm^{-3}	VII 250 J.mm^{-3}	VIII 208 J.mm^{-3}
50	I 417 J.mm^{-3}	II 208 J.mm^{-3}	III 167 J.mm^{-3}	IV 139 J.mm^{-3}

Figure 3. (**A**) Direct sintering strategy, via L-PBF, for the samples generated by different levels of factors ($P_L \times V_S$); and (**B**) compaction system for mixtures in the powder bed.

In the sintering chamber, a continuous 0.3 L.min^{-1} flow of high-purity argon was maintained, and some residual oxygen, estimated at 300 ppm, remained in the chamber. The sintering parameters via L-PBF, as in Figure 3A, for the VED values ($P_L \times v_S$), were based on the research by Uhlmann et al. [28], who investigated the WC-17Co alloy (17% wt. Co), with laser power (P_L) up to 150 W, scanning speed (v_S) up to 100 mm.s^{-1}, line spacing (h_S) below 100 µm and I_Z of 30 and 50 µm (thicknesses). Therefore, it was decided for the WC- and NbC-based alloys with 30% wt. of binder phase, to use the following maximum parameters: P_L up to 125 W, v_S up to 125 mm.s^{-1}and h_S = 80 µm and I_Z = 30 µm. A pneumatic vibrating device created a powder bed with a maximum capacity of 1500 g (proof-of-concept model) with a rubber scraper ruler and a metal roller at the bottom, as in Figure 3B. The speed of the device and the rotation of the roller, as well as the rotation directions, were controlled. The area of the powder bed was enormous (620 cm^2), and the weight applied to the deposited layer was at least 2 kgf (19.6 N). The powder flowed through the bottom of the device, through a stainless-steel sieve, and different mesh sizes could be chosen, depending on the agglomerates' size distribution in the powder mixture [22].

The translational movement of the device simultaneously spread and compacted the powder, creating layers in the powder bed. With the scraper ruler, the layer resulted in 100 µm, and then with the compacting roller, it resulted in a thin and uniform layer of 30 µm. A zigzag scanning strategy was used for a single layer, with a rotation between layers of 67°. The scanning speed varied from 25 to 125 mm.s^{-1}, maintaining a hatch distance (Hs) equal to 80 µm. The laser focal diameter was 140 µm and the compacted mixture layer was 30 µm. For the VED shown in Figure 3A, samples measuring 1.2 × 5 × 5 mm^3 (30 mm^3) were produced, with an average of 40 layers deposited, establishing at least one critical function analytically or experimentally to validate the experiment and proof of concept. Several operational parameters can be associated with this new compaction strategy, such as the clockwise or counterclockwise rotation direction of the compaction cylinder, or in the latter case, with the cylinder locked and controlled to modify the compacted layer in the powder bed (Iz); the effect of the compaction force of the roller on the properties of the powder composites remains one of the main variables.

The processing parameters affect the properties of the granulates: permeability, compressibility, apparent and compacted densities, aeration, elemental flow energy and shear [24]. However, these parameters must be observed in the sintering chamber of the L-PBF process to obtain the critical parameters that demonstrate a direct influence on the performance of the compacted layer in the powder bed and the relationship between the bulk/tapped density. The sintered samples were hard Bakelite, ground with diamond resinoid grinding wheels, grain size 100 µm and grit number W5 (size 3.5–5 µm), with a thickness removal of 0.03 mm, in 2 passes and polished in rotary polishers, with diamond lapping pastes, micron grades: 25, 15, 9, 6, 3 and 1 µm. The apparent porosities were evaluated with 100× magnification and microstructural analysis, 1500× magnification, by optical microscopy Olympus, GX series (Leco Corporation, St. Joseph, MI, USA) Additionally, micrographs of the polished sections were obtained by scanning electron microscopy using both SE and BSE detectors under a high vacuum, Tescan model Vega LMU (TESCAN Group, Kohoutovice, Czech Republic) and Quanta FEI 650 FEG SEM (Thermofisher Scientific, Waltham, MA, USA). For the hardness test, a Vickers hardness tester, Microindentation System, HV-110 series (Mitutoyo, Jundiaí, Brazil), LED lighting system, and motorized load selection system for a 1 kgf (9.81 N) load, HV test, and system A: color LCD touch panel were used.

The analyses of the residual thermal stresses were performed using a Rigaku X-ray diffractometer, model Automate II, (Rigaku Corporation, Osaka, Japan) with X-rays generated by a 2.291Å chromium tube at a voltage of 40 kV and current of 20 mA. The method used was sen2ψ. In the WC samples, the applied modulus was 523.7 GPa, and a Poisson's ratio of 0.22 at an incidence angle of 2θ of 136.63°. For the NbC samples, the elastic modulus was 495 GPa, and a Poisson's ratio of 0.21 at an incidence angle of 2θ of 125.32°. For the WC-based alloys, a hexagonal structure, space group P-6m2, a = 2.9005 Å and c = 2.8290 Å, the peak hkl:(012) was used; and for the NbC-based alloys, an FFC structure, space group Fm-3m, a = 4.47204 Å peak hkl:(222) was used.

XRD measurements were performed on a Rigaku ULTIMA-IV diffractometer (Rigaku Corporation, Osaka, Japan), using Cu-Kα radiation under the following conditions: θ-theta normal scan from 25° to 125°, 0.025° step, 2 s/step, 40 kV, and 30 mA. All the analyses were performed by comparison with the PDF powder pattern databases (Powder Diffraction File from the International Centre for Diffraction Data (ICDD)) or by diffraction patterns calculated from the crystal structure data from the Inorganic Crystal Structure Database (ICSD), American Mineralogist Crystal Structure Database (AMCS) and Crystallographic Open Database (COD) databases, using the Crystal Impact Match and Crystallographica Search-Match software to identify the crystalline phases of the WC, NbC, Co, Ni and other crystalline phases formed.

3. Results and Discussion

3.1. Characterization of Metallic Powders

In Figure 4, the Co and NbC powders present narrow particle size distributions, smaller than 0.1 µm and with a higher percentage of finer particles. Cobalt has a bimodal distribution, where most particles are smaller than 0.1 µm, and a small concentration around 10 µm. This is unlike NbC, which has a normal distribution close to 0.1 µm. This is due to the raw material manufacturing process. In contrast, the other metallic powders, WC and Ni, have larger particles with a more open particle size distribution. The actual density values (pycnometric) of the raw materials are presented in Table 3. They are compatible with the values described in their respective technical data sheets of origin. Co powder has the highest specific surface area compared to other powders.

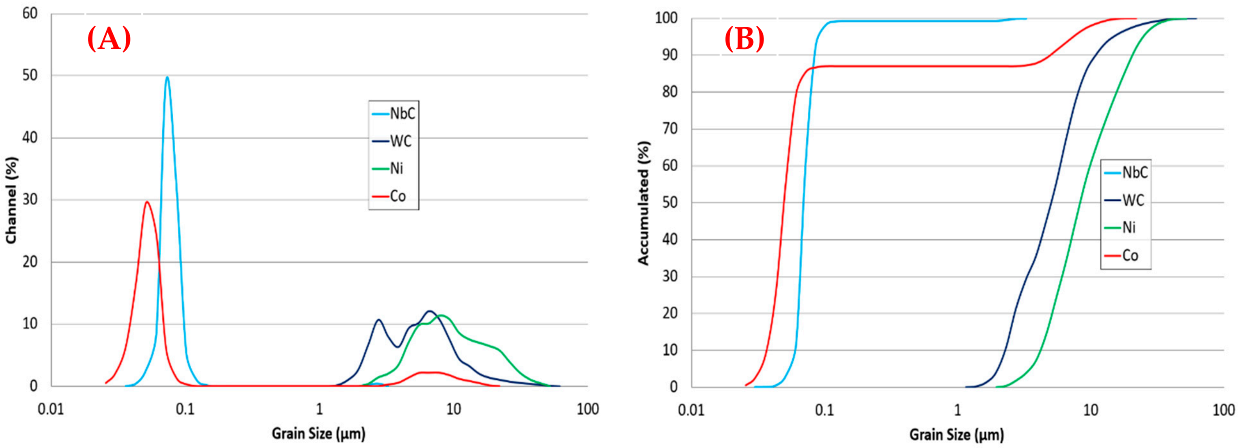

Figure 4. (**A**) Frequency distribution and (**B**) Cumulative distribution of primary particles (NbC, WC, Co and Ni) present in the raw materials, measured by laser diffraction.

Table 3. Characterization of the powders.

Raw Material	Actual Average Density ($g.cm^{-3}$)	Surface Area ($m^2.g^{-1}$)	Total Pores per Volume ($cm^3.g^{-1}$)	Average Pore Diameter (nm)
WC	15.494 ± 0.040	0.624	0.006	35.770
NbC	7.638 ± 0.045	2.586	0.017	26.495
Co	8.422 ± 0.068	4.667	0.015	13.126
Ni	8.952 ± 0.031	1.252	0.012	38.974

To obtain the ideal grid mesh (Tyler equivalent) for the pneumatic vibrating device, the particle size distribution of the powder mixture (WC- or NbC-based composites) is generally considered. However, different characterization methods (sieving and laser diffraction) may provide different results, mainly to obtain the average Sauter diameter (D_{ps}) of the mixture, according to Equation (2) [22], which is considered a valuable property for comparing and controlling the different batches; in this case, for selecting the stainless steel sieve mesh. Here, "D_{ps}" means the mean Sauter diameter (µm), "x_i" is the mass fraction retained in each sieve (dimensionless); and "D_i" is the diameter of the particles retained in each sieve (µm).

$$D_{ps} = \frac{1}{\sum_{i=1}^{n} \frac{x_i}{D_i}} \tag{2}$$

The sieving method is the most widely used in industries that manufacture cemented carbide products. The particle size distribution of WC- and NbC-based alloy agglomerates is an important process variable that, associated with the selected sieve mesh, directly affects the flowability and powder deposition rate. It depends on the particle size of the raw materials but also on the cohesion of the particles that form the granules, which in turn results from several factors, such as the density, specific surface area, roughness and moisture. In Figure 5A,B, the Sauter diameter D_i is calculated from Equation (2), resulting from the knowledge of the particle size distributions of the WC- and NbC-based samples, where the average particle size of the mixtures was obtained. In Figure 5A, the test for 200 g, the indicated mesh was the Tyler equivalent #140 (100 µm); in practice, with the pneumatic device, there was a flowability of the powders in the container. However, for Figure 5B, the test with 1000 g, the Tyler equivalent meshes that flowed the mixtures in the studies were the #35, #50, and #60 meshes. When comparing Figure 5A,B, it is seen that the frequency and cumulative distributions of the agglomerated particles of the dry powder mixtures behaved differently, interfering in the aggregation of the solid particles; consequently, the Sauter D_{ps} values were other results in the mass transfer. The Sauter D_{ps} is used in studies related to interfacial phenomena. The evaluation of the particle size distribution of powdered composites is essential in all the processes proposed for producing sintered parts, as it is intrinsically linked to the density and linearity/volumetric shrinkage.

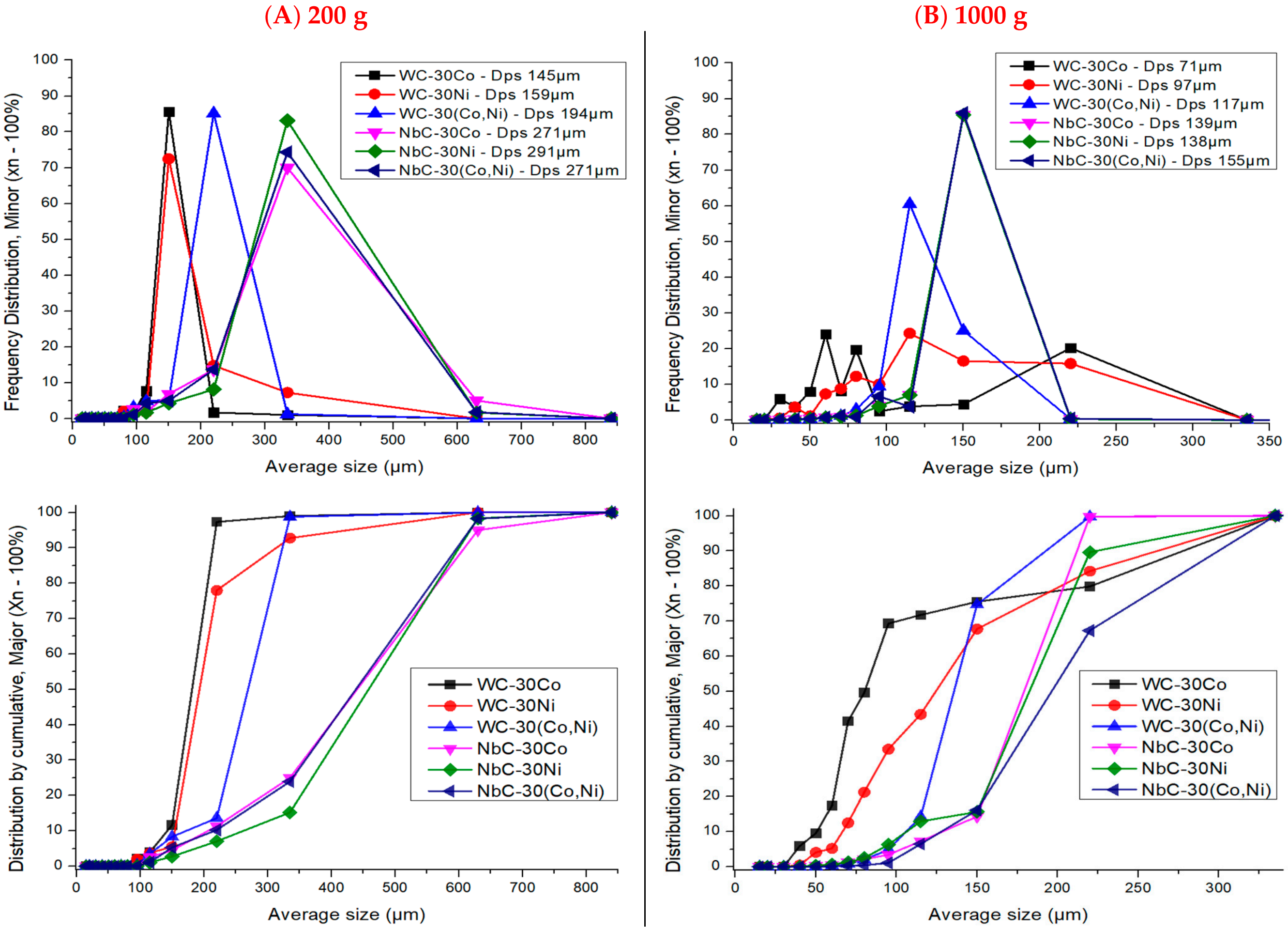

Figure 5. Frequency distribution and cumulative distribution of the agglomerated particles of the dry powder mixtures: (**A**) 200 g and (**B**) 1000 g, which correspond to the material to be deposited by the device.

Using the FT-4 Powder Rheometer® equipment, the basic flow energy (BFE), stability, and variable flow (VRF) tests were carried out, measuring the resistance to the passage of a blade through the particle bed. The sample stability was evaluated under constant rotation of 100 mm.s^{-1} (blade tip speed of 48 mm diameter) as a function of time (number of tests from 1 to 7); the torque and force were recorded and converted into flow energy. The movement of the blade through the bed of particles can modify the packing, the interactions between the particles and alloy mixtures, or even cause surface modifications: abrasion, breaks, segregation, etc. The basic flow energy (BFE) is the value of the total energy that the blade expends, measured in the seventh test after the samples have stabilized. It can be seen in Figure 6A that in the seventh test, a level of stability is observed, ensuring the reliability of the measurement of this parameter.

In general terms, in Figure 6, the energy required to move the bed of refractory WC particles is more significant in the samples containing predominantly NbC; this occurs because the density of WC (15.494 g.cm^{-3}) is higher than that of NbC (7.638 g.cm^{-3}), and more energy is needed to move denser particles. Additionally, for the samples with the same majority component (WC and NbC), Table 4 shows that the samples containing only Ni are those that require the most significant amount of energy to be moved by the blade; that is, the mechanical transport of both materials containing only Ni in their composition is more complicated. The incorporation of Co in the samples containing only Ni reduces the basic flow energy (BFE). Using only Co proves to be more effective in reducing the flow energy of the samples. Therefore, Co appears to act as an attenuator of interparticle interactions, allowing more effortless movement of powder bed particles. To eliminate the effect of the density of each type of material on the energy consumed by the blade when crossing the powder bed, we can divide the BFE by the mass of material that constitutes the powder bed, resulting in the flow energy per gram of material moved: the BFE/mass of the material. Thus, the effort per unit of mass required to move the WC and NbC samples with only Ni in their composition appears practically identical. Adding Co together with Ni is not significant for the WC samples. However, the energy reduction observed when adding only Co to the samples is evident, especially for the NbC samples, in Table 4.

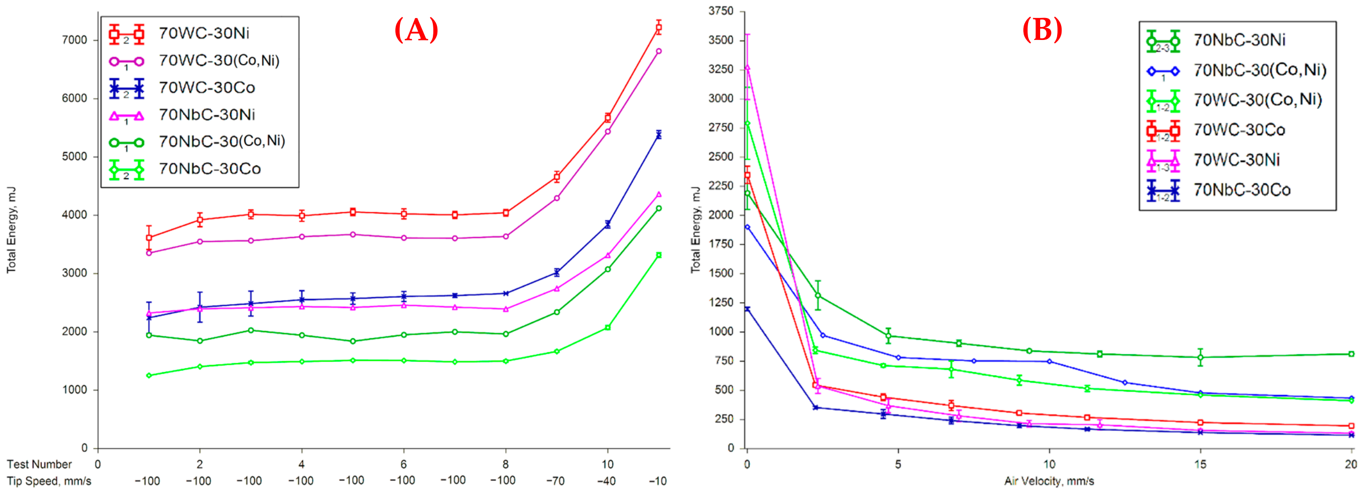

Figure 6. (**A**) Test of the basic flow energy (test number 1 to 7) and variable flow energy (test number 8 to 11) and (**B**) aeration test of the WC- and NbC-based mixtures.

Table 4. BFE and VFR test results: relationship between the bulk and compressed density (BD) and the applied pressure.

Composition	BFE (mJ)	SI	SE (mJ.g^{-1})	Split Mass (g)	BFE.g^{-1} (mJ.g^{-1})	BD (g.cm^{-3})	CPS 15 kPa	BD$_{comp.}$ (g.cm^{-3})
WC-30Co	4007.11	1.11	6.87	634.31	6.317	3.33	9.13	3.66
WC-30Ni	3606.39	1.08	7.96	564.88	6.384	4.11	6.29	4.39
WC-30(Co, Ni)	2623.04	1.18	6.61	507.74	5.166	3.60	9,74	3.99
NbC-30Co	2424.98	1.04	7.80	377.95	6.416	2.45	13.08	2.82
NbC-30Ni	2001.91	1.03	8.31	332.56	6.020	2.47	14.32	2.88
NbC-30(Co, Ni)	1486.77	1.19	5.70	375.78	3.956	2.21	14.42	2.59

An interesting test is the aeration test, as shown in Figure 6B, which is essentially the basic flow energy (BFE) test with air injection at the base of the sample bed. It measures the reduction in interactions between particles (reduction in the BFE) as a function of the amount of air injected into the system. As part of the volume initially occupied by a solid is now occupied by air, the blade exerts less effort to go through the bed of particles. Thus, the air separates the particles to allow them to pass. When the energy stabilizes, the lowest state of interaction between the particles is reached, and the bed reaches its fluidization condition. Furthermore, if the particles are not cohesive, they separate easily, and the layer can permeate the bed without significant difficulties, reaching levels at shallow values. For particles that still present specific interactions (cohesiveness), the same level is reached at higher air flow rates or higher levels for the same flow rates. Table 4 presents the results of the basic flow energy (BFE) for all the powder samples, as well as the results of the compressibility tests at 15 kPa. The complete evaluation of the compressibility behavior of all the samples, when subjected to normal stresses ranging from 0.5 to 15 kPa, is exhibited in Figure 7B. Table 5 presents the results of the shear cell experiments conducted at 3, 6, 9, and 15 kPa of consolidation stress.

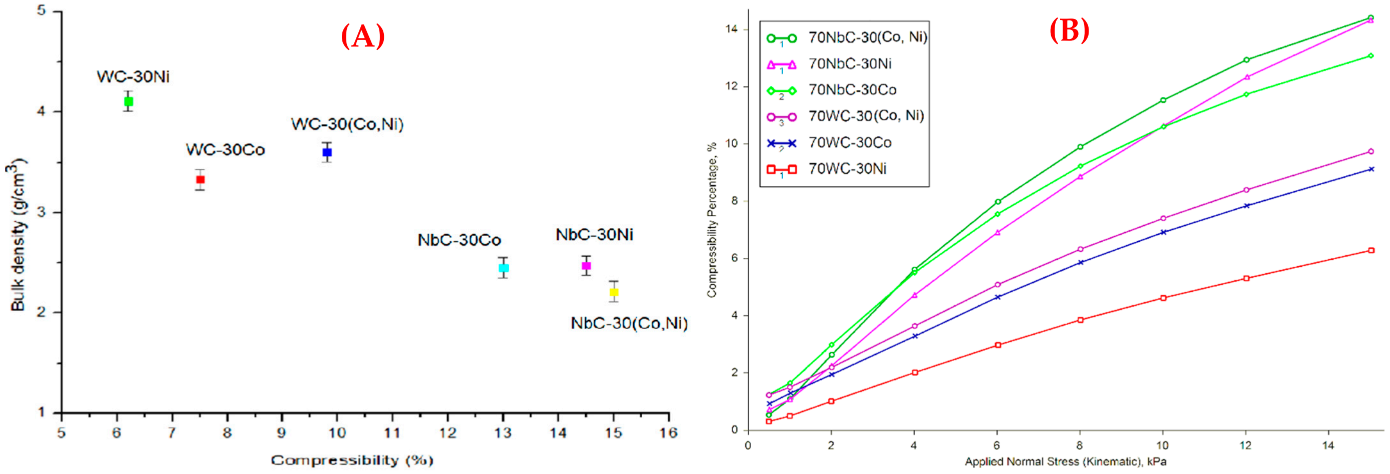

Figure 7. (**A**) Bulk density (BD_{comp}); and (**B**) compressibility tests of the WC- and NbC-based alloys.

Table 5. Shear test results: cohesion and angle of internal friction (AIF) under different stress conditions.

Composition	3 kPa		6 kPa		9 kPa		15 kPa	
	Cohesion (kPa)	AIF (°)	Cohesion (kPa)	AIF (°)	Cohesion (kPa)	AIF (°)	Cohesion (kPa)	AIF (°)
WC-30Co	0.73	32.4	1.16	32.9	1.45	33.1	1.66	34.4
WC-30Ni	0.62	31.8	1.06	31.9	1.35	32.9	1.44	35.8
WC-30(Co, Ni)	0.96	32.5	1.39	33.7	1.82	33.7	2.08	36.3
NbC-30Co	0.69	29.4	0.93	31.7	1.19	31.0	1.23-	32.4
NbC-30Ni	1.31	35.7	1.90	40.4	-	-	2.96	42.2
NbC-30(Co, Ni)	1.09	32.7	1.56	33.4	2.07	33.7	2.04	37.1

Figure 7 demonstrates that the NbC samples are more compressible (percentage change in volume after compression, %) than the WC samples, regardless of the addition of other compounds. Thus, it is possible to state that the WC samples have lower porosity, producing a bed of particles with fewer voids, with the sample being WC-30Ni. This means that the granulation of the NbC samples must be further worked to reach the same state of compaction as the WC samples. The small oscillations between points 1 and 3 for samples of alloys WC-30Ni, WC-30(Co, Ni), WC-30Co, and NbC-30Co, as in Figure 6, indicate an initial accommodation of the samples in the bed, which stabilize from the third test. Observing the cohesion values of the samples, Figure 8 shows that the WC-30Ni sample is the most cohesive, corroborating the aeration test results and the primary flow energy per unit mass (BFE.g^{-1}). The WC-30Ni and NbC-30Co samples had the lowest cohesion values, corroborating the aeration and basic flow energy per unit mass (BFE/g) tests. Shear tests also allow for the so-called flow function of materials, which classifies their flow profile. The results indicate complete fluidization of all the samples at an air velocity of 15 mm.s^{-1} (for a diameter of 50 mm) but a significant reduction in the BFE at low flow rates (2.5 to 5.0 mm.s^{-1}). Significantly reduced cohesion is observed for the samples containing only Co, whereas the most excellent cohesion is observed for the NbC-30Ni samples, as in Figure 8. The samples containing Ni and Co appear to present two levels of energy stabilization. This may indicate two moments of fluidization, the first for smaller particles (fines) and the second for the remaining particle size (analyze the particle size distribution and check if it is bimodal). An important observation is the behavior of the samples containing Ni, which shows that the mixture is more cohesive than the mixture containing NbC; however, it presents the lowest cohesion when mixed with WC. This indicates that interactions between different elements are essential for the flowability of the studied samples. The flowability of powders is not an inherent property—it depends not only on the physical properties (shape, particle size, moisture content, etc.) but also on the stress state, on the equipment used, and on the handling method. The powder flow in individual additive technology methods is a complex area of study [29]. Figure 8A,B show the shear stress test and flow profile classification of the WC- and NbC-based alloys, respectively, indicating once again that the NbC-30Ni sample exhibits the most cohesive and difficult-to-flow behavior. Adding Co to the sample enhances its flow properties, with both samples containing a mixture of Co and Ni exhibiting similar behavior. The WC-30Ni sample demonstrates the most favorable flow characteristics among the samples containing only Co. Achieving the reliable flow of cohesive powders presents a significant challenge in various particle-processing operations, including silo and hopper unloading, feeding, dosing, etc., whereby the shear strength is evaluated under specific consolidation stress or packing conditions. Typically, this evaluation involves moderate to high stresses and meager shear strain rates [30].

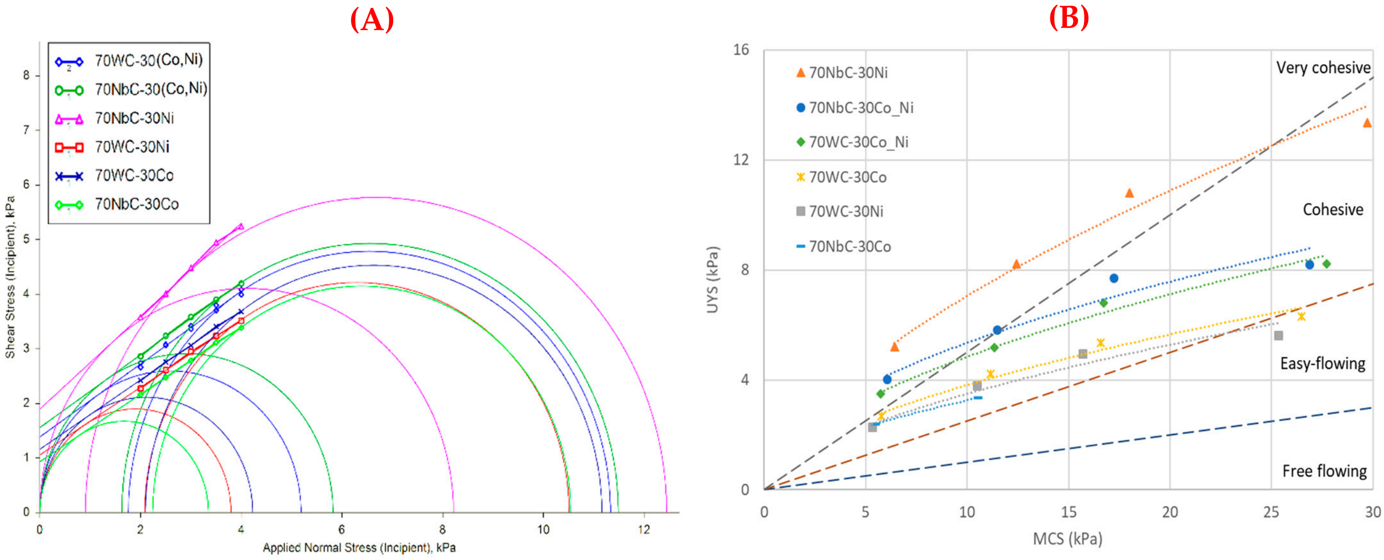

Figure 8. Shear stress test for the quantitative measurement of cohesion; (**A**) 6 kPa and (**B**) classification of the flow profile of WC- and NbC-based alloys.

In additive manufacturing via L-PBF, this dry powder deposition technique is promising, with the advantage of being applicable to small quantities of powder composites based on WC and NbC in the vibrating device. However, further investigation into its behavior in the dynamic regime is necessary, with more significant measurement repetition, to better differentiate between powders with similar rheological properties in all the packing states. This type of dry granulation is not suitable or the most commonly used for processing techniques via L-PBF; it is more often used for conventional sintering techniques via LPS. No information in the literature indicates which formulation properties are suitable or unsuitable for this processing method. The qualities of the parts manufactured by additive manufacturing (AM) are influenced by the characteristics of the powders, which include the shape, size distribution, surface morphology, composition, and flowability or flowability of the particulates [31].

The typical particle sizes for sintering via L-PBF are in the range of 10 to 60 µm. The behavior of a composite/ceramic powder is fundamental to its performance in the manufacturing process, such as in compaction, in which the filling operations of molds or die powder spreading depend on the flowability. Various methods or tests can help with the evaluation of dynamic flow and flowability. Still, specifying the best flow condition is not always clear, given that different sizes and shapes correlate [32]. In the AM technique, the experimental characterization is minimal when measuring composite properties, such as the average diameter, particle size distribution, and packing density. It is inadequate to solve a specific configuration for powder bed deposition [31,32]. Powdered composites used for AM are spread onto a compacted layer for direct sintering, and this process is repeated from layer to deposited layer to form the product. The measurement techniques used to evaluate the powder flowability can be divided into separate categories [3], such as the flow rate, density rates, bulk and beat density, angle of repose, and shear stress, among other methods [1–3].

The difference between these methods can be significant, as the test method affects the stress state and velocity of the particulates, the bulk density, the tapped density, and other factors that influence the feed flow behavior [31,32]. These flowability methods for powders have been known for a long time and are recommended for AM. In general, the physical behavior of powders directly influences the manufacturing process parameters via L-PBF; the main properties are the shapes of the particles, the distribution and size of the grains, the apparent density, the thickness of the deposited layers, and the properties of the powder composites [33].

The packing of powders can be quantified based on their bulk/tapped density. Flowability tests allow for obtaining the mass flow rate and the bulk density [22]. Some tests promote a denser random packing, allowing the accumulated air (in the particulates) to escape through agitation and the settling of the powders, which is performed with a constant volume [32]. Dry granulation in compaction techniques is unsuitable for all powder materials. Binders are needed to make this conventional processing method suitable. However, the quality of the dry granulate is known to significantly impact the compaction processes, which is shown to be a function of the rheological properties of the granules. In turn, other studies have found that powders with the same particle size can have very different flow behavior due to the effects of other properties, such as the texture, surface shape, and accumulation [24].

3.2. Volumetric Flow Rate Test of NbC- and WC-Based Alloy Mixtures

According to the ASTM normative definitions, the volumetric flow rate allows for controlling the mass (process) and height of the delicate layers in the powder bed (quality). The flowability is a function of some parameters: the particle size distribution, particulate or agglomerate size, cohesive strength, friction between particles, and particle morphology. For this reason, the tests reported in Section 3.1 are indispensable. Among the standards available for determining the flowability of powders for additive manufacturing, the Hall flowmeter is the most widely used, being relevant for systems that use pipes, dozers, or powder injectors in the sintering chambers, assuming that they are spherical particles and free-flowing. However, the Carney flowmeter funnel is recommended for cemented carbide powders or mixtures that do not flow freely. Regarding the pneumatic vibrating device, the importance of the flow rate, or the volumetric flow rate, is related to the time required to fill the volume in the powder bed, avoiding waste and shortages in the construction of the powder bed [22].

The deposition and displacement speed of the device needed to achieve a uniform flow of the metal powder mass are factors with significant influence in terms of the L-PBF technique. For the volumetric flow test of the WC- and NbC-based mixtures, the device was used in a stationary mode outside the sintering chamber. The mass flow results are presented graphically as a function of the device vibration (Figure 9). For this new mass flow test or measurement methodology, an average quantity of 1300 g of powder was placed in the container to flow by gravity and by vibration of the device, varying the pressure in the system from 0.25 MPa (460 Hz), 0.30 MPa (490 Hz), and 0.35 MPa (520 Hz), with the selection of the #35 mesh sieve, the empirically ideal one as predicted in the particle size distribution test (Figure 5). The WC-based samples presented higher bulk density values than the NbC-based alloys and presented a longer flow time under a pressure of 0.35 MPa (520 Hz). The pressure of 0.25 MPa (460 Hz) resulted in uneven stacking layers forming in the powder bed, which is not recommended. The best ability of the mixtures to flow within the vibrating device is a function of the particle shapes, which increase the friction between the particles; the higher the friction, the lower the flow rate of the powder mixtures in the powder bed [22].

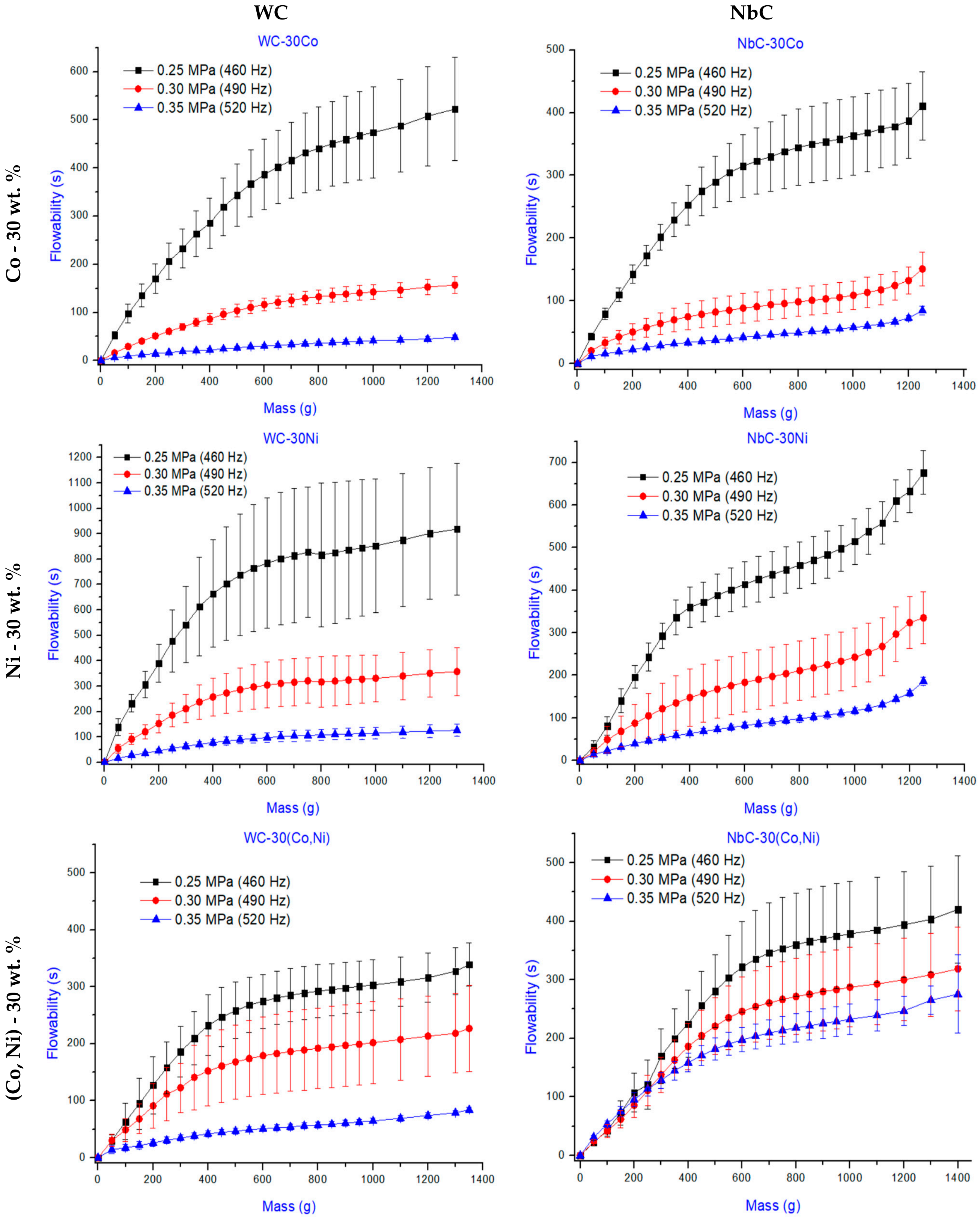

Figure 9. The mass flow rate of the WC- and NbC-based powder mixtures for a #35 mesh sieve as a function of the system pressure or container vibration frequency [22].

The mixtures containing Ni presented the most challenging flow behavior. Within the small range of the standard deviation of each mass flow curve, the data tend to be more concentrated around the mean; that is, the flow is uniform and contributes to a homogeneous layer in the powder bed. The pressures of 0.35 MPa (520 Hz) presented the best results, except for the NbC-30(Co, Ni) alloy; that is, the values of the dataset are equal to the means, without much variation.

The NbC-30(Co, Ni) alloy presented a high variance value for all the pressures in the system, indicating that the observed values tend to be far from the mean, which can cause failures in the deposition layers in the bed. In the stage of spreading the mixtures on the powder bed using only the scraper ruler, the deposition layers in the first preliminary tests presented irregularities and a lack of adhesion between the mixed particles, as shown in Figure 10A.

Figure 10. Flow rate and spreadability behavior of mixtures in the powder bed, as a function of the system pressure or device vibration frequency: (**A**) lack of adhesion between particulates; (**B**) craters and "alligator shell" and (**C**) uniform, homogeneous, and continuous flow from the central part of the powder bed.

With the compacting roller rotating clockwise and counterclockwise, craters appeared on the surface of the powder of the "alligator shell" type, as in Figure 10B. However, with the roller locked, it filled the gaps created by the scraper ruler well, making the deposition layer uniform. For this reason, controlling the mass flow rate versus the flow time to control the speed of the vibration device transfer is inevitable. In addition, there was a significant improvement in the densification, going from a condition of bulk density to a beaten or pressed density, as in Figure 10C.

An important observation in this test is that for values below 0.20 MPa, specifically for a #35 mesh sieve, the powder did not flow and the particles settled or packed together. For a pressure of 0.40 MPa, large quantities of the powder were expelled through the upper part of the container; therefore, mass flow curves were not performed. For the powder spreadability, the displacement speed of the pneumatic device varied from 40 to 60 mm.s^{-1}. The moisture in the mixtures greatly influenced the flowability behavior, reducing the flow rate. To avoid this setback, heating the powder at 100 °C for 2 h in an oven was standardized for all the mixtures to perform this test, and the same conditions were performed in another period for the direct sintering process [22].

Another important feature of the dry granulation of powder mixtures with metal rollers is that it is widely applied in the pharmaceutical industry; it can continuously produce large quantities of compacted granular products at a comparatively low cost. Two of the main advantages of this process are that it is dry and continuous. Despite being a simple process, a quantitative understanding of the process has been challenging due to the complex behavior of the particulate materials, which can result in unsatisfactory linear compactions [26].

3.3. Porosities and Microstructures of WC- and NbC-Based Alloys via L-PBF

The samples from the L-PBF technique had dimensions of 1.0 × 5.0 × 5.0 mm (25 mm^3), equivalent to 40 deposition layers for all the WC- and NbC-based alloys. The apparent porosity analyses were performed using a light microscope (100× magnification), as determined by ASTM B276 [34]. Figure 11 shows the porosity characteristics of the WC- and NbC-based samples based on the power parameters (W) as a function of the scanning speeds ($mm.s^{-1}$). In this case, the apparent porosities are classified as type A, which are microporosities below 10 μm, and type B, which are microporosities between 10 and 25 μm; above 25 μm, they are classified as macro porosities. There is also the classification of type C, which represents free or uncombined carbon. Type B and type C porosities can impair the sintered cemented carbide alloys' mechanical properties with binder phases ranging from 3 to 30% by weight. Electrolytic etching was necessary to analyze the microstructures of the WC- and NbC-based alloys, as shown in Figure 12. Due to the high corrosion resistance of cemented carbide alloys, 5 volts were applied for 5 s in the presence of the Murakami solution: 10 g of potassium ferrocyanide K_3 $[Fe(CN)_6]$ and 10 g of sodium hydroxide (NaOH) dissolved in 100 cm^3 of distilled water. An optical microscope (OM) was used to observe the microconstituents, with magnifications of up to 1500×, according to ASTM B657 [35]. The standard test method for the metallographic determination of the microstructure of cemented carbides was applied to identify the eta-η phase (W_3Co_3C) and α-phase (WC), with fine, medium, and coarse structures, respectively [36].

In addition to revealing the grain boundaries of WC and NbC, the abnormal grain growth of the WC- and NbC-based alloys is evidenced [36,37]. The presence of fine-, medium- and coarse-grain W_2C carbides (heterogeneous structure), together with the eta-η phase, for the WC-30Co/WC-30(Co, Ni)-based alloys embrittles the material. The same occurs for other WC- and NbC-based alloys combined with Ni. Increasing the content of the binder phase in the initial mixture can reduce the incidence of cracking in cemented carbides produced by the L-PBF technique. However, increasing the Co content in cemented carbide alloys would significantly increase the manufacturing cost and decrease the hardness of the sintered product [38].

No scientific or technological study has been able to produce WC-based cemented carbides without defects by additive manufacturing in a single direct sintering step. In addition, direct sintering with a high-power laser, above 200 W, causes Co evaporation, WC decomposition, and carbon loss, among other undesirable effects, such as the formation of the embrittlement phases, W_2C and Co_3W_3C, which are inevitably formed in the rapidly solidified microstructure. Other studies have already indicated that pores can form due to gases in the molten pool as the volumetric energy density (VED = $J.mm^{-3}$) increases, resulting in undesirable effects such as keyholes [39]. Anomalies occurred in the structures of the WC- and NbC-based alloys during direct sintering with rapid cooling, as shown in Figure 13 A to H. Figure 13A shows the lack of fusion and microcracks in the WC-30Ni alloy, with parameters of P_L = 50 W; v_S = 100 $mm.s^{-1}$ and VED = 167 $J.mm^{-3}$. In Figure 13B, gas was trapped during solidification, resulting in spherical pores. In Figure 13C, there are transgranular and intergranular cracks in the WC-30Co alloy, with parameters of P_L = 75 W; v_s = 25 $mm.s^{-1}$ and VED = 625 $J.mm^{-3}$. Figure 13D highlights the presence of the η-phase (W_3Co_3C), which contributes to the generation of macro- and microcracks. In Figure 13E, the top view of sample V of the WC-Co alloy (VED = 625 $J.mm^{-3}$) shows sintered tracks (laser beam direction), thermal cracks, and the heat-affected zone (HAZ), as well as the heterogeneous structure. Figure 13F has the same image of the same region as Figure 13E, without attack, evidencing only the cracks due to thermal or internal residual stresses. Figure 13G, an enlarged region of Figure 13E, evidences the mixed interface and HAZ, with cobalt lakes and abnormal WC grain growth, and Figure 13H shows evaporation of the binder phase.

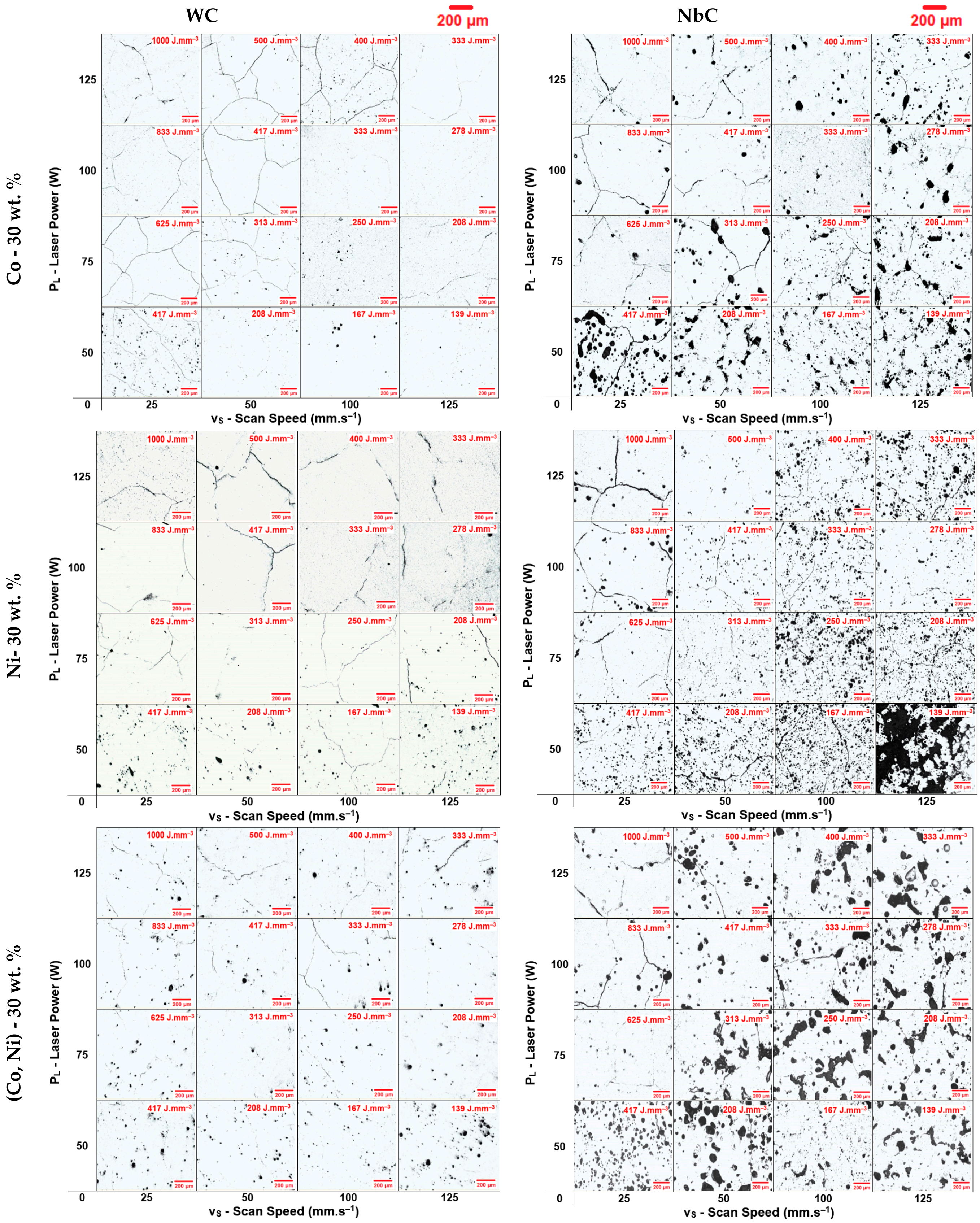

Figure 11. Characteristics of the apparent porosities (MO—100×) of the WC- and NbC-based cemented carbide samples generated by different levels of energy factors, VED ($P_L \times v_S$), adapted from [36,37].

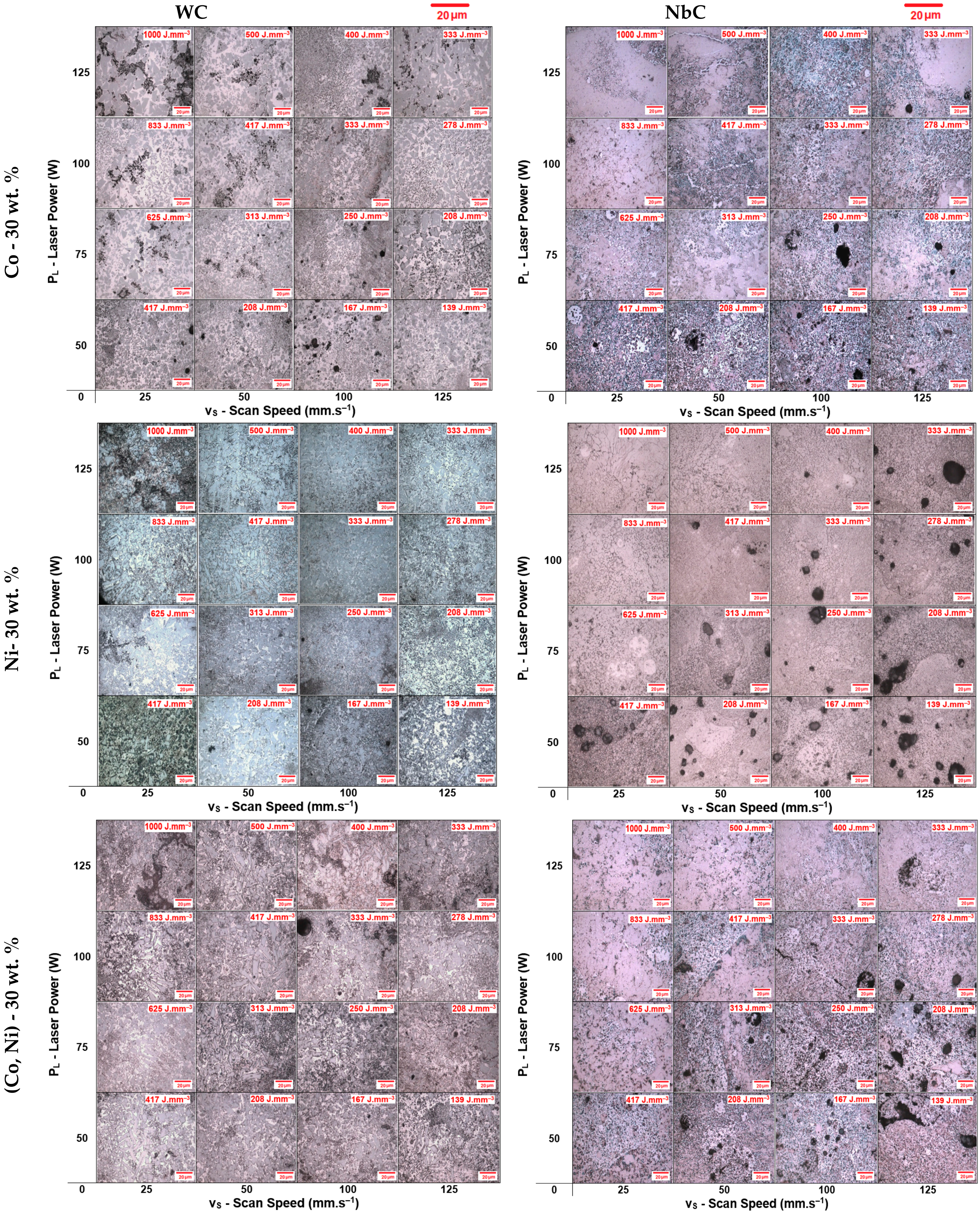

Figure 12. Characteristics of the microstructures (MO—1500×) of the WC- and NbC-based cemented carbides samples generated by different levels of energy factors, VED ($P_L \times v_S$), adapted from [36,37].

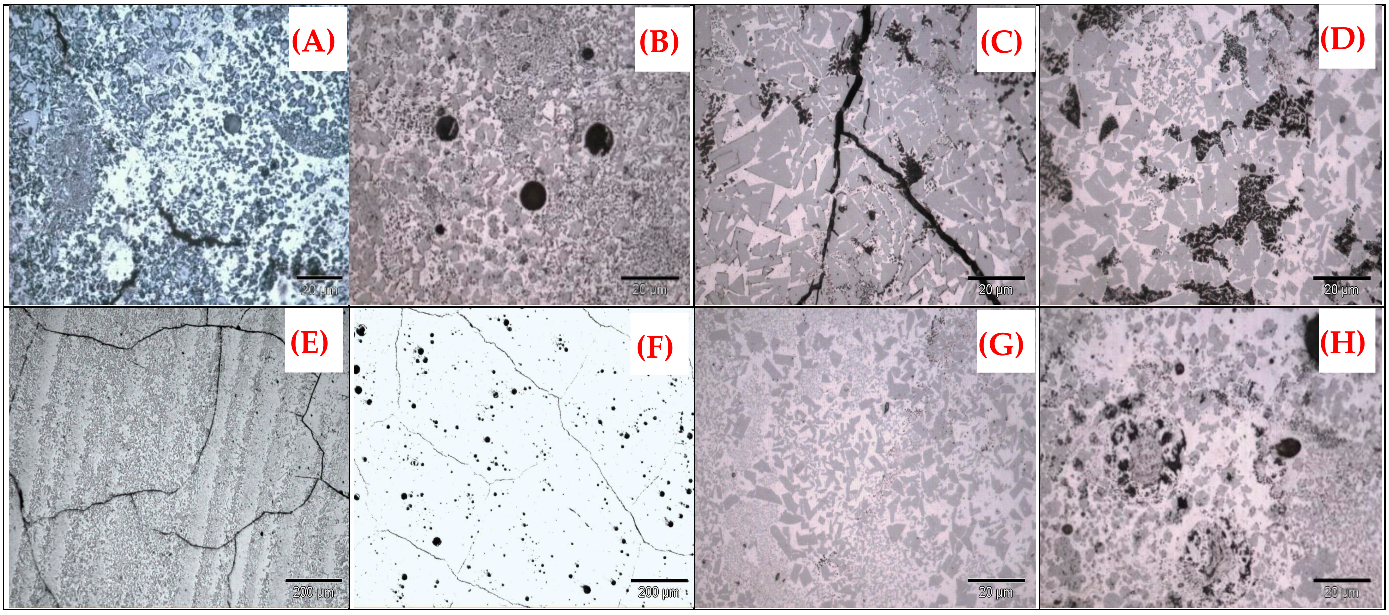

Figure 13. Micrographs (OM): (**A**) Lack of fusion between the sintered layers; (**B**) spherical pores originating from trapped gases; (**C**) transgranular cracks (binder phase); (**D**) eta-η phase (W_3Co_3C); (**E**) unmixed deposited tracks with HAZ (heterogeneous structure); (**F**) thermal cracks and macro pores; (**G**) Co lakes and abnormal WC grain growth; and (**H**) evaporation of the binder phase.

In the case of WC-Ni-based alloys, there was WC impoverishment to W_2C, with a rounded and non-hexagonal prismatic shape. The loss of carbon changes the densities of the alloys, and the hardness is reduced significantly. WC particles, which are directly exposed to a laser beam, are disintegrated into tungsten and carbon due to the excess energy [37]. The leading cause of the η-phase appearing in the test specimens is the presence of oxygen inside the sintering chamber. Even with the dynamic continuous flow of argon (0.3 $L.min^{-1}$) in the system, the total elimination of oxygen is impossible. As the carbon content depends on the sintering atmosphere, the carbon weight balance cannot be fully controlled and decarburization occurs. However, uncertainties arise in the control of microstructures, considering the appearance of $WC_{0.5}$ (called β-W_2C, hexagonal compact HC) and the stable form WC (6.14 wt.% C, face-centered cubic phase—(FFC) [39,40]. Abnormal WC growth can compromise the product's performance. For example, it can contribute to premature wear of cutting tools or machining inserts, which should be avoided. Refined or sub-micron WC grains are the most desirable microstructural feature in these cases. However, coarse grains can be interesting for mechanical forming tools subjected to impact, whereby higher toughness is required. This mechanism is not fully understood, which justifies the lack of research on this abnormal grain growth for the L-PBF [36]. In Figure 14, the microstructures (BSE-SEM images) of WC-based alloys with 30 wt.% of binder phase, sintered by the conventional LPS route (1370 °C) and L-PBF, are compared for the sample parameters: XI (P_L = 100 W × v_s = 100 $mm.s^{-1}$) and XVI (P_L = 125 W and v_s = 125 $mm.s^{-1}$). Almost complete dissolution of WC is observed in the liquid phase and during supercooling, with the precipitation of secondary carbides and abnormal growth of particulates. The greater the supercooling in the binder phase, the easier the nucleation of columnar grains and equiaxed dendrites in the region rich in the binder phase.

The formation of the metastable η-phase for the WC-Co alloys is possibly due to its lower surface energy than WC, meaning that its formation would be energetically favored at relatively low cooling rates. Still, at relatively fast cooling rates, the amount of transformation is severely limited, resulting in a high fraction of retained eta-η phase and relatively few abnormal WC grains. The lack of complete carburization of the eta-η phase can be explained by kinetic limitations [41]. The decrease in the carbon mass fraction leads to the formation of the ƞ phase due to carbon deficiency. There are two types of eta-η phase. The first is M_6C, which forms at equilibrium temperatures above 1150 °C. The second, $M_{12}C$, forms at temperatures below 1150 °C. In the samples obtained via L-PBF, the two types of eta-η phase resulted for the $(W, Co)_6C$ and $(W, Co)_{12}C$ samples [42]. The abnormal growth occurs as the eta-η phase is carburized during solidification to form WC and expel Co, as in Figure 15, following the reaction:

$$Co_4W_2C + C \rightarrow 2WC + 4Co \tag{3}$$

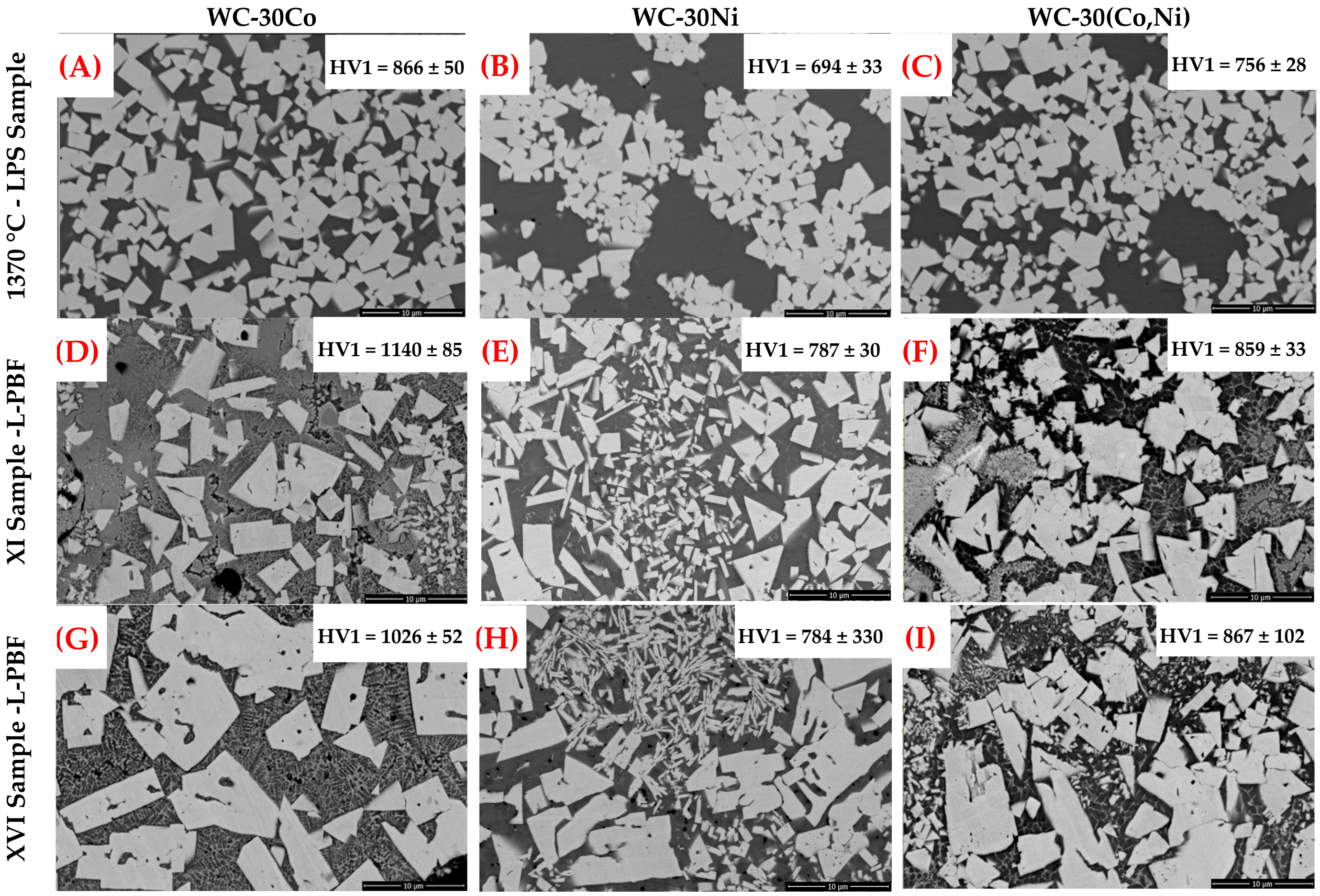

Figure 14. (**A**) WC-30Co, (**B**) WC-30Ni and (**C**) WC-30(Co, Ni) produced by the LPS conventional route [36], 1370 °C; BSE-SEM images corresponding to: (**D**) WC-30Co alloy, (**E**) WC-30Ni alloy (**F**) WC-30(Co, Ni) alloys samples XI (P_L = 100 W × v_S = 100 mm.s^{-1}). BSE-SEM images (**G**) WC-30Co alloy, (**H**) WC-30Ni alloy (**I**) WC-30(Co, Ni) alloy samples XVI (P_L = 125 W × v_S = 125 mm.s^{-1}), via L-PBF.

For the WC-Co- and WC-Ni-based alloys, the presence of carbon not combined with W in the chemical composition can result in the presence of type C porosity (free carbon, θ-phase) in the binder phase of the sintered products, according to ASTM B276 [36], which makes the product brittle and reduces the mechanical properties, especially for commercial grades G4, G5 and G6, alloys with 20, 25 and 30 wt.% binder phase, respectively. However, a lack of carbon can lead to the formation of carbon-poor carbide (W_2C) in the WC-Ni alloy, which in turn partially reacts with Ni to form Ni_2W_4C (ternary carbide). Finally, controlling the carbon content of the WC-Ni alloy mixtures prevents the formation of these compounds, and their harmful effect is on the densification during direct sintering [43]. Few studies have been reported on manufacturing cemented carbides and cermets using L-PBF techniques, mainly alloys with high binder phase contents. The few reported or published works have evidenced the formation of cracks, abnormal growth of WC grains, heterogeneous structures, decarburization, and composition alteration, resulting in the degradation of the mechanical properties [44]. Table 6 compares the chemical composition of the 70WC-30Co and 70WC-30(Co, Ni) alloys of samples XI and XVI with their respective direct sintering parameters. Table 6 allows observation of the loss of carbon and the evaporation of the metallic phase. For the WC provided in Table 1, the percentage of combined carbon is 5.8 wt.% C, and for NbC, it is 7.8 wt.% C.

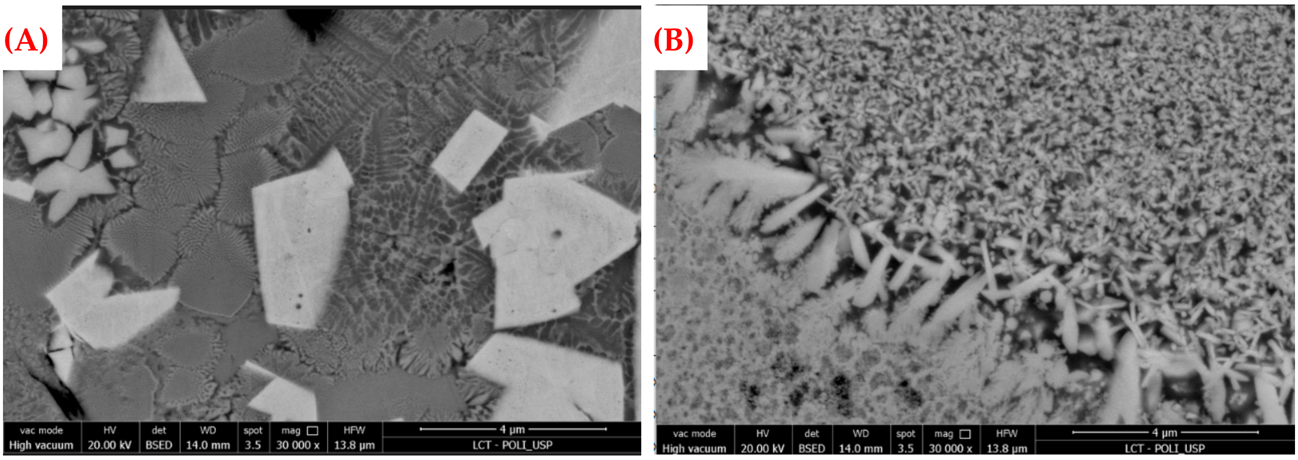

Figure 15. BSE-SEM images corresponding to (**A**) WC-30Co, sample XI, Figure 14D primary dendrites of Co (hypoeutectic structure) with the presence of eta-η phase dendrites; and (**B**) WC-30(Co, Ni), sample XVI, Figure 14F WC carbides in the form of secondary dendrites at the interface between the layers with the precipitation of small WC grains in the alternative binder phase (Co, Ni).

Table 6. Comparison of the chemical composition of samples sintered via L-PBF.

Material	Sample	Parameters	VED (J.mm^{-3})	C (wt.%)	Co (wt.%)	Ni (wt.%)	W (wt.%)
70WC-30Co 70WC-30(Co, Ni)	XVI	P_L = 125 W v_s = 125 mm.s^{-1}	333	5.054445 4.655052	23.11550 14.71521	- 12.20967	71.83005 68.42006
70WC-30Co 70WC-30(Co, Ni)	XI	P_L = 100 W v_s = 100 mm.s^{-1}	333	4.319959 5.784030	30.20653 16.73984	- 13.10717	65.47351 64.36896

When the VED value is very high, above VED = 300 J.mm^{-3}, the microstructures of the WC-Ni-based samples revealed WC grains of different sizes and shapes, with a heterogeneous distribution, as shown in Figure 16. Figure 16A shows that it is difficult to identify what occurs in the binder phase solid solution via OM, when compared with SEM images, as in Figure 16B,C: the WC precipitates, or WC reinforcement in the metal matrix, or binder phase; the qualitative nature of segregation is shown, respectively, with a maximum and a minimum for WC and Ni. Both resources, OM and SEM images, are necessary for better structural identification. Out-of-equilibrium conditions tend toward high micro segregation, WC diffusion, and WC reinforcement (by precipitation) in the Ni metal matrix due to the high VED values leaving brittle structures with refined WC grains and low binder phase content for Ni-based alloys. Nb-C has a wide range of stoichiometric carbon and hexagonal Nb_2C in the binary diagram, from approximately 6.8 wt.% C to 11.8 wt.% C, resulting in NbC_{1-x} + C_{free} [21].

In the Nb-C equilibrium diagram presented by Labonne et al. [8], unlike W-C (with 6.0 wt.% C), presented by Garcia et al. [21], compounds such as NbC_{1-x}, Nb_2C, $Nb4C_{3-x}$ or Nb_6C_5 can be formed. Therefore, the amount of carbon will strongly influence the structure of NbC-based cemented carbides [8]. NbC and Nb_2C carbides are stable but have very different crystal structures, respectively, cubic and hexagonal. The chemical bond of NbC is very complex, with a predominant covalent characteristic, but it also presents metallic and ionic characteristics [15].

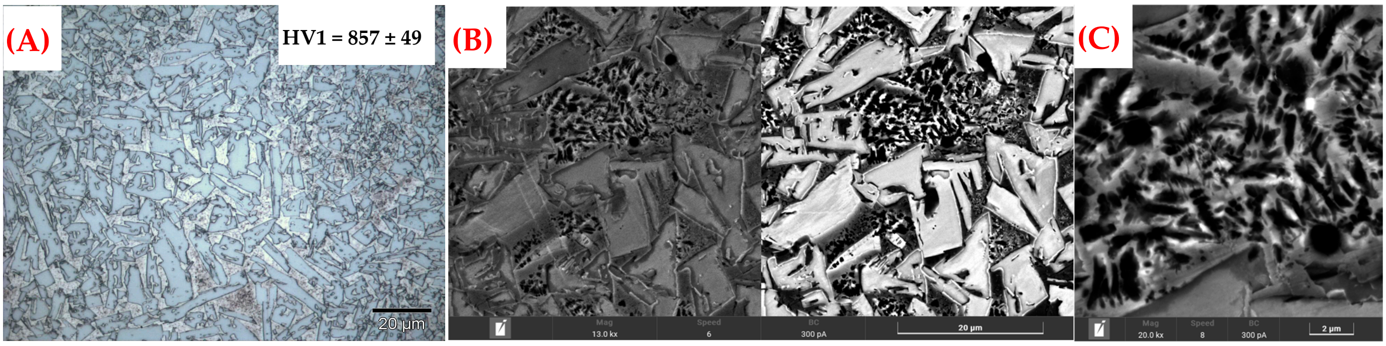

Figure 16. (**A**) OM (1500×) of the WC-30Ni alloy, parameters: P_L = 125 W, v_s = 100 mm.s^{-1} and VED = 400 J.mm^{-3}; (**B**) BSE-SEI (13,000×) with coarse and abnormal hexagonal grains of the WC-30Ni alloy, highlighting the light region WC, SEI image (right); and (**C**) BSE-SEM (20,000×) dark region, reinforcement of the binder phase by the precipitation of Ni interdendritic eutectics.

For producing NbC-based cermets with Ni, Co, or combined binder phases obtained by the conventional route (indirect sintering), Figures 17 and 18 point out that there is abnormal grain growth for the NbC-30Ni and NbC-30(Co, Ni) alloys, which reached average sizes of 9.0 ± 5.0 µm and 7.0 ± 2.0 µm, respectively, after LPS sintering at 1370 °C for 30 min of stabilization, starting from NbC particles smaller than 1 µm. This shape of the WC grains, and for NbC, can be obtained in different ways; useful strategies include adjusting the production parameters (time and temperature) for conventional carbides [45] so that WC grains can be made spherical or faceted prisms [21]. To inhibit this uncontrolled growth, considering sintering via LPS, secondary carbides are added [8,13,14]. In this case, 3 wt.% WC was added to the NbC-based alloys, aiming to obtain a finer and more homogeneous microstructure, with excellent hardness, and then compared with the samples sintered via L-PBF, as in Figures 19–21.

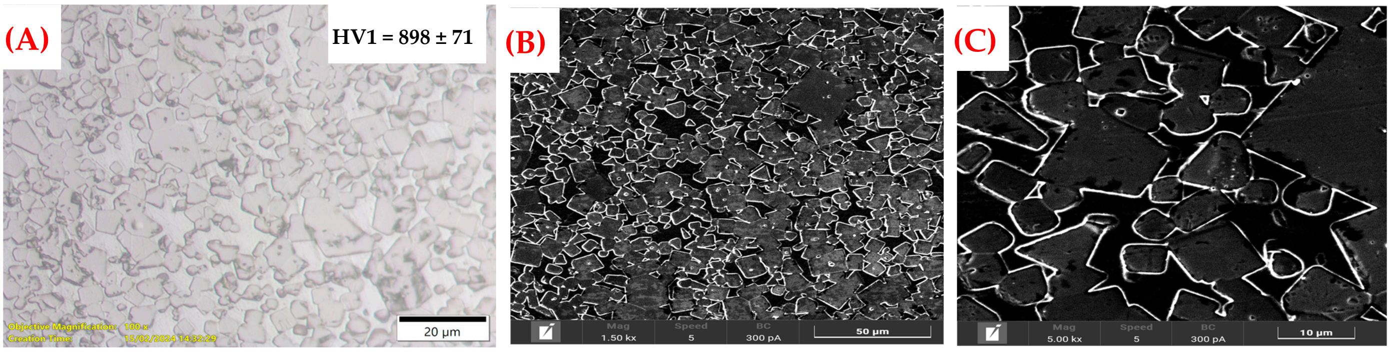

Figure 17. Microstructures of the NbC-based carbide, NbC-30Ni alloy, sintered conventional LPS route (1370 °C, 30 min, and 50 MPa); (**A**) OM image—1000× magnification; (**B**) BSE-SEM—1500× magnification; and (**C**) BSE-SEM—5000× magnification.

Adding these secondary carbides significantly improves the wettability of the liquid phase among the ceramic phases, improving the densification of the sintered material. These small additions should vary from 0.25 to 3.0 wt.%; WC, VC, Mo_2C, TaC, and Cr_2C_3 are commonly used in cermets to inhibit NbC grain growth [12]. Both Co and Ni binders have good wettability for NbC and can dissolve a significant amount of carbide in the liquid state, 4.8 wt.% for Co and 3.9 wt.% for Ni [8]. Another important observation is related to the different stable and unstable phases, pseudocubic, NbC, Nb_4C_3, and Nb_6C_5, that can modify the stoichiometry of NbC_X during sintering, allowing significant variations in the mechanical and microstructural properties, because of a wide range of 6.8 to 11.8 wt.% C, as shown in the Nb-C binary phase diagram by Labonne et al. [8], for forming NbCx ranging from $0.75 \leq x \leq 1.0$ at the ratio x = C/Nb [46]. Figures 17 and 18 allow observation that even with the addition of 3 wt.% WC, there was considerable coalescence and growth of the NbC grains. The growth behavior of the NbC grains is therefore dependent on the addition of secondary carbides and the combined carbon content [47].

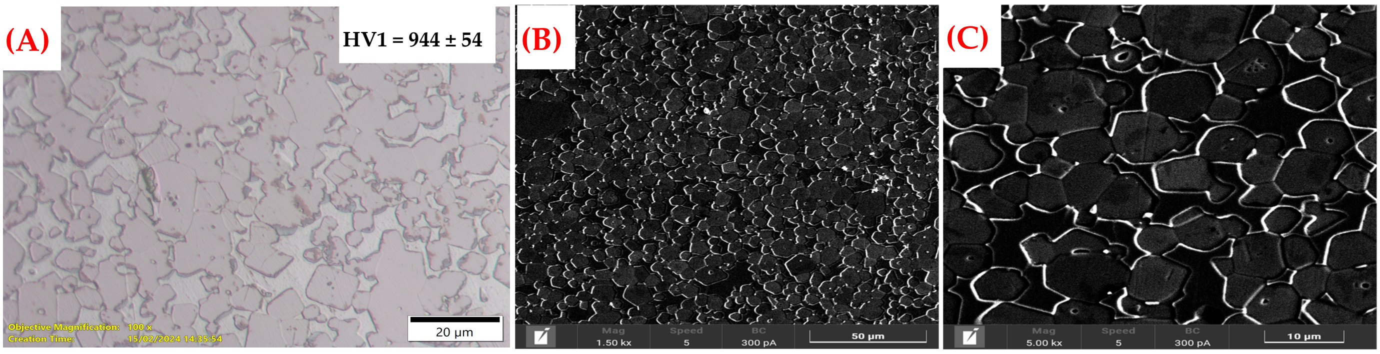

Figure 18. Microstructures of the NbC-based carbide, NbC-30(Co, Ni) alloy, sintered via conventional LPS route (1370 °C, 30 min, and 50 MPa); (**A**) OM image—1000× magnification; (**B**) BSE-SEM—1500× magnification; and (**C**) BSE-SEM—5000× magnification.

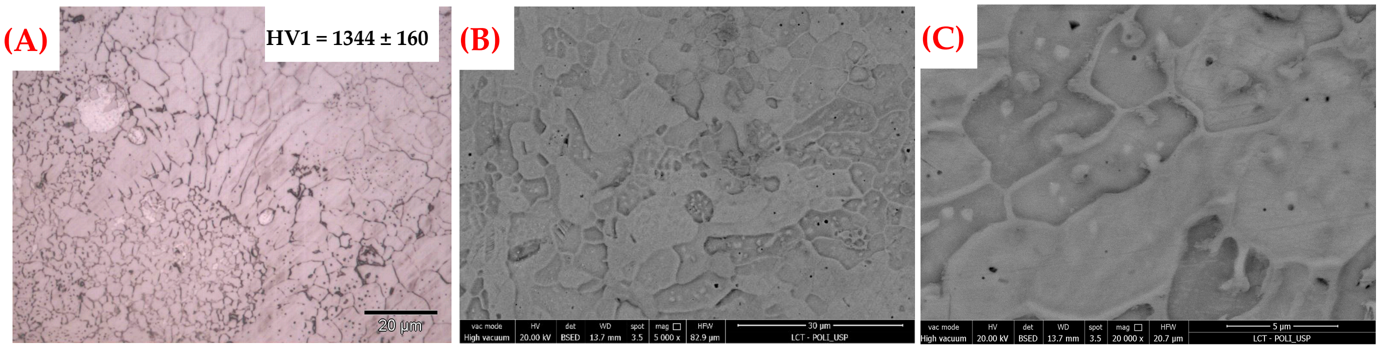

Figure 19. Microstructures of the NbC-30Ni alloy, sintered via L-PBF, sample XIII with parameters: P_L = 125 W, v_s = 25 mm.s^{-1} and VED = 1000 J.mm^{-3}. (**A**) OM image, 1500×; (**B**) FEG–SEM image—5000×; and (**C**) FEG–SEM image, 20,000×.

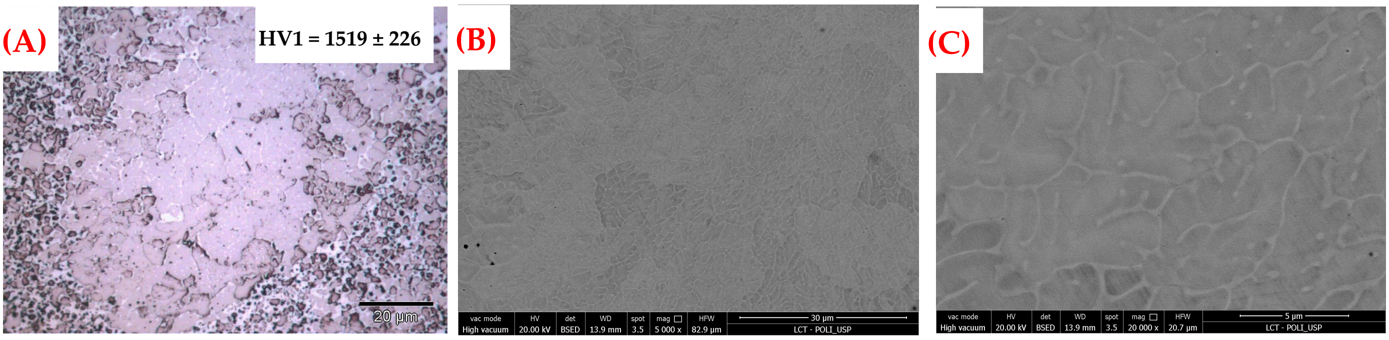

Figure 20. Microstructures of the NbC-30Co alloy, sintered via L-PBF, sample XIII with parameters: P_L = 125 W, v_s = 25 mm.s^{-1} and VED = 1000 J.mm^{-3}. (**A**) OM image, 1500×; (**B**) FEG–SEM image—5000×; and (**C**) FEG–SEM image, 20,000×.

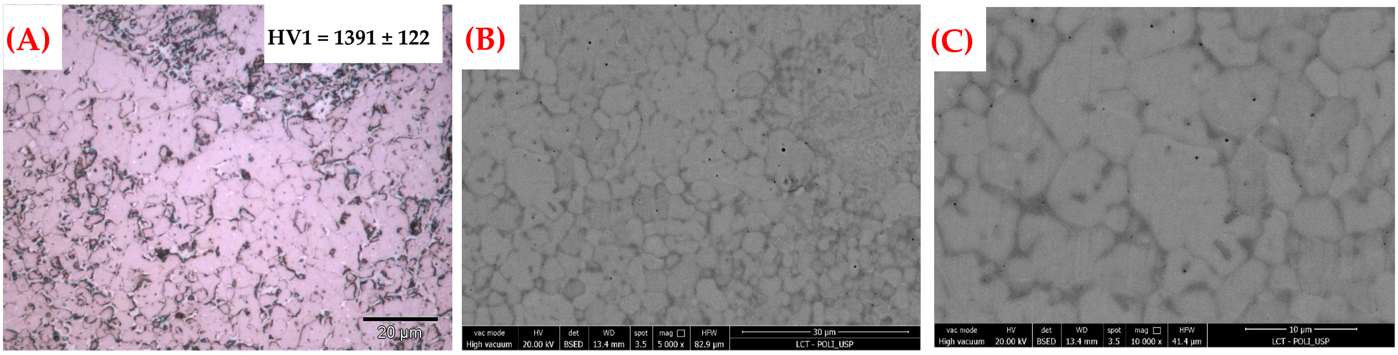

Figure 21. Microstructures of the NbC-30(Co, Ni) alloy, sintered via L-PBF, sample XIII with parameters: P_L = 125W, v_s = 25 mm.s^{-1} and VED = 1000 J.mm^{-3}. (**A**) OM image, 1500×; (**B**) FEG–SEM image—5000×; and (**C**) FEG–SEM image, 10,000×.

The distribution of the NbC grains was heterogeneous in the microstructures of the NbC-30Ni, NbC-30Co, and NbC-30(Co, Ni) alloys, sintered via L-PBF for samples XIII, with the highest energy VED = 1000 J.mm^{-3}. Observing Figures 19A, 20A and 21A, it is clear that there are limitations in evaluating the contiguity of the NbC phase regarding the use of the OM for 1500× magnification. Better visualization of the NbC/binder phase interaction is achieved by using SEM; notably, there is the formation of a skeleton (coalescence and growth of adjacent grains), the contiguity is much more significant, and abnormal NbC grains are consequently predominant in the microstructure; few areas of the binder phase are observed, which does not occur with WC-based alloys. Trapping of the inclusions of the binder phase inside the NbC_X is evidenced in the NbC-30Ni alloy, as in Figure 19C. For a better understanding of the formation of the resulting phases for the NbC-based alloys, the characterization by X-ray diffraction (XRD) results in an average model for the structure of the material, which, for technological applications, allows for determining whether the developed alloys satisfy the requirements for a given application. The direct sintering technique is characterized by rapid heating and cooling, and the solubility or dissolution of the WC and NbC particles in the molten zone during laser scanning is inadequate or interrupted. Consequently, the W, NbC, and C elements dissolved in the Co and Ni binder phases, or their combination (Co, Ni), undergo in situ synthesis, forming ceramic reinforcement phases or the secondary carbides WC and W_2C in the binder phase. The refractory elements WC and NbC diffuse into the molten zone and react with the Co and Ni elements to generate metallic carbide phases. Therefore, it is essential to determine that the X-ray diffraction (XRD) patterns of the samples align with the thermodynamic calculations [48].

3.4. Microhardness of WC- and NbC-Based Alloys via L-PBF

Table 7 provides the microindentation hardness data of the WC- and NbC-based alloys as a function of the L-PBF sintering strategy for the different VED levels. The Vickers hardness test determined the hardness with a load of 9807 N (1 kg). Ten indentations on each sample were made to determine the average hardness of the samples with their respective standard deviations. A Vickers hardness using 1 kgf of load is noted as HV1. The hardness values available in the literature and the commercial catalogs of cemented carbide product manufacturers indicate a range of HV 700 to 1000 for the traditional WC-30Co alloy, designated as grade G6/G7. This is a classic grade of cemented carbides with great prominence and application in the steel industry as cylinders, roll rings, torsion rolls, rollers, and guide rollers [16,21,49]. This hardness range depends on the average grain size of the WC. For the Vickers hardness tests, the HV is 0.2 to HV 100, according to the ISO 3878 standard [50].

Table 7. Vickers hardness by the microindentation of WC- and NbC-based alloys as a function of the sintering strategy via L-PBF for different factor levels ($P_L \times v_S$).

Sample	**P_L (W)**	**Vs (mm.s^{-1})**	**VED (J.mm^{-3})**	**WC**			**NbC**		
				30Co (wt. %)	**30Ni (wt. %)**	**30(Co, Ni) (wt. %)**	**30Co (wt. %)**	**30Ni (wt. %)**	**30(Co, Ni) (wt. %)**
I	50	25	417	983 ± 33	585 ± 147	778 ± 66	1152 ± 111	518 ± 127	991 ± 289
II		50	208	943 ± 98	762 ± 49	832 ± 93	989 ± 115	595 ± 228	735 ± 164
III		100	167	862 ± 148	701 ± 172	818 ± 93	884 ± 135	589 ± 74	694 ± 215
IV		125	139	798 ± 168	565 ± 97	783 ± 62	875 ± 104	577 ± 62	543 ± 115
V	75	25	625	1186 ± 73	625 ± 50	873 ± 55	1162 ± 232	895 ± 164	1110 ± 193
VI		50	313	1348 ± 83	788 ± 72	734 ± 96	1227 ± 220	808± 179	937 ± 155
VII		100	250	940 ± 116	739 ± 90	907 ± 57	1124 ± 206	644 ± 137	905 ± 132
VIII		125	208	1113 ± 69	779 ± 52	835 ± 120	1138 ± 153	815± 164	1032 ± 131
IX	100	25	833	1242 ± 80	756 ± 84	893 ± 69	1482 ± 238	1013± 214	1409 ± 161
X		50	417	1270 ± 40	793 ± 29	867 ± 84	1318 ± 131	1089 ± 158	1235 ± 163
XI		100	333	1140 ± 85	787 ± 41	859 ± 33	1130 ± 136	777 ± 224	1135 ± 215
XII		125	278	1059 ± 36	819 ± 67	838 ± 70	1134± 121	668 ± 134	992 ± 158
XIII	125	25	1000	1216 ± 64	672 ± 34	865 ± 43	1519 ± 226	1344 ± 160	1391 ± 122
XIV		50	500	988 ± 69	758 ± 71	842 ± 49	1241 ± 202	1087 ± 222	1322 ± 213
XV		100	400	1093 ± 103	803 ± 32	857 ± 49	1179 ± 140	897 ± 168	1063 ± 274
XVI		125	333	1026 ± 52	784 ± 30	867 ± 102	1157± 182	605 ± 102	851 ± 237

For grades with 30 wt.% Co binder, with extra-coarse grains, the average hardness is equivalent to 690 HV10 (81 HRA), with a density of 12.75 g.cm^{-3}, and for a grade with 30 wt.% Co-Ni-Cr, the hardness is equivalent to 610 HV10 (80 HRA), with a density of 12.70 g.cm^{-3}. These are cemented carbide grades with high binder content, exhibiting toughness and good thermal shock resistance, mainly of medium- to extra-coarse WC grain size used under demanding mechanical, thermal, and often chemical operating conditions. The mechanical and thermal loads in these applications, such as hard metal tools and hot rolling, are highly dynamic. There is a growing trend toward extra-coarse WC grains in mining and construction applications to profit from the higher fracture toughness and thermal conductivity [49]. For other average Vickers hardness values, the classical WC-30Co alloys presented ranges of 900–1000 HV30 (refined grains) and 750–850 HV30 (medium grains), respectively [51].

A marked increase in the average microhardness of the samples based on WC and NbC with the Co binder phase is noticeable, with values above HV1 1000. Combined with the results of the analysis of the microstructures WC-30Co in Figure 15A and NbC-30Co in Figure 20, this evidences the diffusion of the refractory elements WC and NbC to the binder phase, contributing to the precipitation of carbides' refined grains from the solid solution. Additionally, there is some evaporation of the binder phase (change in chemical composition) and an increase in the microhardness of the binder phase due to the segregation and emergence of dendrites and the formation of embrittlement compounds, such as the η-phase. There is a gradual decline in microhardness, as observed in alloys based on WC and NbC containing Ni in the binder phase, as in Table 7, taking the hardness properties relatively below the minimum value of 700 HV1. Decarburization, abnormal carbide growth, and the formation of the W_3Ni_4 compound are the probable causes of this undesirable effect. The only grade that maintained the hardness results in the range of 700 to 1000 HV1 was the WC-30(Co, Ni) alloy.

3.5. Thermal Residual Stresses of WC- and NbC-Based Alloys via L-PBF

Thermal residual stresses play an essential role when cracks are evidenced in the samples, mainly in sintering via the L-PBF technique followed by rapid cooling. They arise due to the difference in thermal expansion between the binder phase and the carbides [49]. Due to the large number of samples, the following samples were selected for residual stress analysis: IV (VED = 139 J.mm^{-3}); VII (VED = 250 J.mm^{-3}); X (VED = 417 J.mm^{-3}) and XIII (VED = 1000 J.mm^{-3}), according to the $P_L \times v_S$ strategy, as in Figure 3A, for the WC- and NbC-based cemented carbide alloys, as shown in Figure 22A,B, respectively.

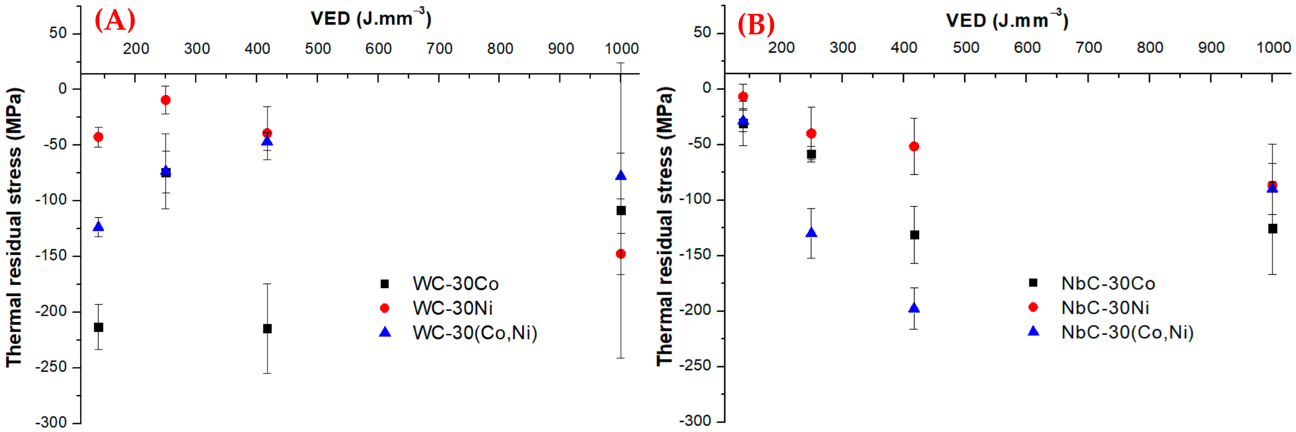

Figure 22. Comparison of the residual thermal stresses (compressive), after polishing, for the L-PBF samples: IV (VED = 139 J.mm^{-3}); VII (VED = 250 J.mm^{-3}); X (VED = 417 J.mm^{-3}) and XIII (VED = 1000 J.mm^{-3}); (**A**) WC-based alloys; and (**B**) NbC-based alloys.

The results show a tendency toward compressive residual stress on the surface of the samples, in general, ranging from −10 MPa to −220 MPa for the WC-based alloys and from −10 MPa to −200 MPa for the NbC-based alloys, which are compressive stresses, as shown in Figure 22A,B. The thermal residual stresses in the polished samples of the WC-based and NbC-based alloys containing Ni, for energies below VED = 417 J.mm^{-3}, are observed to be significantly lower when compared to the WC-based and NbC-based alloys containing Co and (Co, Ni), except for VED = 1000 J.mm^{-3}. Also verified is that the tendency toward higher residual thermal stresses (compressive) is related in the WC- and NbC-based samples containing Co [37]. The uncertainties of the measurements of the polished samples, for energies VED = 1000 J.mm^{-3}, are higher, as seen in all the WC- and NbC-based samples. Due to the temperature gradient between the sintered layers N, N-1, and N-2 during direct sintering for various VEDs, varied thermal expansions and contractions (linear/volumetric) occur in the rapid cooling, which cause distortions and compressive and tensile stresses [37,48]. The residual compressive stresses on the surface of the samples resulted in tensile stresses somewhere below the surface, as in Figure 23A. The internal stresses (tensile versus compressive) can separate the material sintered via L-PBF from the substrate, resulting in horizontal and vertical cracks, or only vertical, which results in slower crack growth, as shown in Figure 23B,C [38].

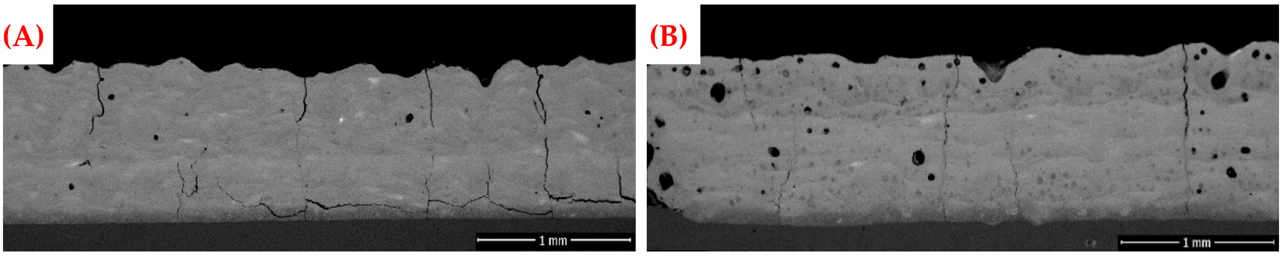

Figure 23. (**A**) FEG–SEM image (100×) of sample X of the NbC-30Co alloy, parameters P_L = 100 W, vs = 50 mm.s^{-1} and VED = 417 J.mm^{-3}; and (**B**) SEM image of sample XIII of the NbC-30(Co, Ni) alloy, parameters: PL = 125 W, vs = 25 mm.s^{-1} and VED = 1000 J.mm^{-3}.

Another hypothesis for the occurrence of microcracks during direct sintering via L-PBF of Co-containing hard metal alloys is that Co (100 wt.%, pure) is allotropic; above 427 °C, it presents a face-centered cubic (FCC) crystalline structure and, upon supercooling, its structure changes to ε-Co hexagonal compact (HC), whereas nickel (FCC), remains a FCC upon supercooling. Therefore, Co can present two allotropic forms, ε(HC) and α(FFC). For combining Co and Ni in the proportion 1:1, a solid solution FCC (α-Co, Ni) is obtained after the allotropic transformation of ε-Co FCC. The Co alloy can present a stable cubic crystalline structure from certain levels at high temperatures, 760 to 980 °C, or even at room temperature [42]. The powder bed substrate was manufactured in AISI 1020 steel (0.2%C) due to the manufacturing cost and the fact that it has a different thermal expansion coefficient from cemented carbides, and this may have contributed to the increase in thermal residual stresses and generation of cracks in the WC- and NbC-based samples.

3.6. Phase Composition Analysis via XRD

Since there are several phase modifications in the microstructures, as seen in Figures 14–21, it is essential to identify the phases, via XRD, for different factor levels ($P_L \times v_S$), which can be used in the metallurgical industry and in the area of materials sciences, both for the conventional LPS route and for AM [52]. For better phase identification, a sample sintered by the conventional LPS route at 1370 °C for 30 min in a vacuum furnace at 2×10^{-5} mbar was compared, which served as a reference standard. Due to the large number of samples available, samples XIII sintered via L-PBF, with parameters of P_L = 125 W, v_S = 25 mm.s^{-1} and VED = 1000 J.mm^{-3}, which presents the highest VED level, were selected for the XRD studies for comparison purposes. Figure 24 compares the results of samples XIII (L-PBF) with samples sintered via LPS, which presented significant differences, as the sintering via L-PBF leads to the formation of new phases and the partial decomposition of chemical compounds. These phase changes in the WC- and NbC-based alloys occurred due to the decreased carbon and evaporation of the metallic binder phase (Co and Ni).

This topic details the critical compositional changes that occur during the direct sintering process for the highest VED (1000 J.mm^{-3}) for WC- and NbC- based alloys with Co and alternative Ni and (Co, Ni) binder phases. As observed in Figure 24, all the diffractometry peak points in the XRD patterns were identified. In the WC- and NbC-based samples containing (Co, Ni), particularly for the WC-30(Co, Ni) and NbC-30(Co, Ni) alloys, the metallic binder phase is noted to be practically a single phase in solid solution, the FCC binder phase marked as α-(Co, Ni). For the samples containing only the Co binder phase, the WC-30Co and NbC-30Co alloys, sintered via L-PBF and conventional LPS route, in the XRD, a compact hexagonal HC form is evidenced, ε-Co (COD ID 9011617); and another part transformed into the FCC form, α-Co (COD ID 9011619), allotropic transformation. An important observation is that the mixing and homogenization process was carried out with a simple mixer (homogenizer), not by ball milling or attrition milling, which can mechanically induce this transformation from α-Co to ε-Co [53].

The ε-Co is transformed into α-Co above 427 °C, as seen for both sintering techniques (LPS and L-PBF), as in Figure 24. However, during cooling, the reverse transformation can occur, with α-Co transforming into a hexagonal form; two modifications occur: α-Co and ε-Co [42,53]. When comparing the diffractograms of the WC- and NbC-based alloys, the peaks of the significant carbides, WC (COD ID 2102265) and NbC (COD ID 9008682), are notable for the samples sintered via LPS and L-PBF. However, for the WC-30Co-based alloys sintered via L-PBF, the presence of W_2C (COD ID 1539792), $W_9Co_3C_4$ (COD ID 1528857), and Co_7W_6 (COD ID 1528857) is noticeable due to the carbon deficiency in the carburization process to obtain WC (carbothermal reaction during the mixing of carbon black), the carbon combined with W is well below 6.14%wt (theoretical), and the decarburization during sintering, LPS (<50 ppm O_2) and L-PBF (~300 ppm O_2).

Peaks of new phases were observed, as shown in Figure 24, possibly indicating small intermetallic phase formations of Co_7W_6 (COD ID 1524837), Co_3W (COD ID 1524836), Co_2Nb (COD ID 1525052), Co_7Nb_6 (COD ID 1525267), and new carbides: CNi_3 (COD ID 1563177) e Co_2C (COD ID 1528415), and high amounts of eta-η phase. Intermetallic phases and ternary phases are key factors in the mechanical properties of cemented carbides [54], especially for high-temperature or high-energy sintering (J.mm^{-3}). The resulting phases of the W-C-Co ternary phase diagram system are very complex, and the possible phases include eta-η phases (Co_6W_6C and Co_3W_3C), di-tungsten carbide (W_2C) and the intermediate phase Co_7W_6 [55]. Chicinas et al. [56] state that traditional WC-Co alloys with low carbon content, in magnetization tests, suggest the formation of carbon-deficient phases (M_6C and $M_{12}C$) and that the eta-η phases are not magnetic and that their formation is influencing the total magnetic saturation, as given by the fraction of free Co. WC-Co alloys containing sub-carbide phases, M_6C and $M_{12}C$, are of interest for cutting tools, as they potentially increase wear resistance. To achieve this, the growth of the eta-η phase needs to be controlled by finely dispersing them and preventing them from agglomerating. For WC-based alloys with a high binder phase content, with applications in the steel industry, the formation of these large and brittle sub-carbides must be avoided [56,57]. The letter "M" represents the metallic phase and can be Ni, Co or W in varying amounts, for example, M_6C in WC-Co cemented carbides range from $Co_{2.2}W_{3.8}C$ to Co_2W_4C and for $M_{12}C$, Co_6W_6C to $Co_{5.9}W_{6.1}C$. The M_6C phase appears above 1150 °C. After cooling, M_6C transforms into the $M_{12}C$ phase and both have FCC crystal structures [55,58].

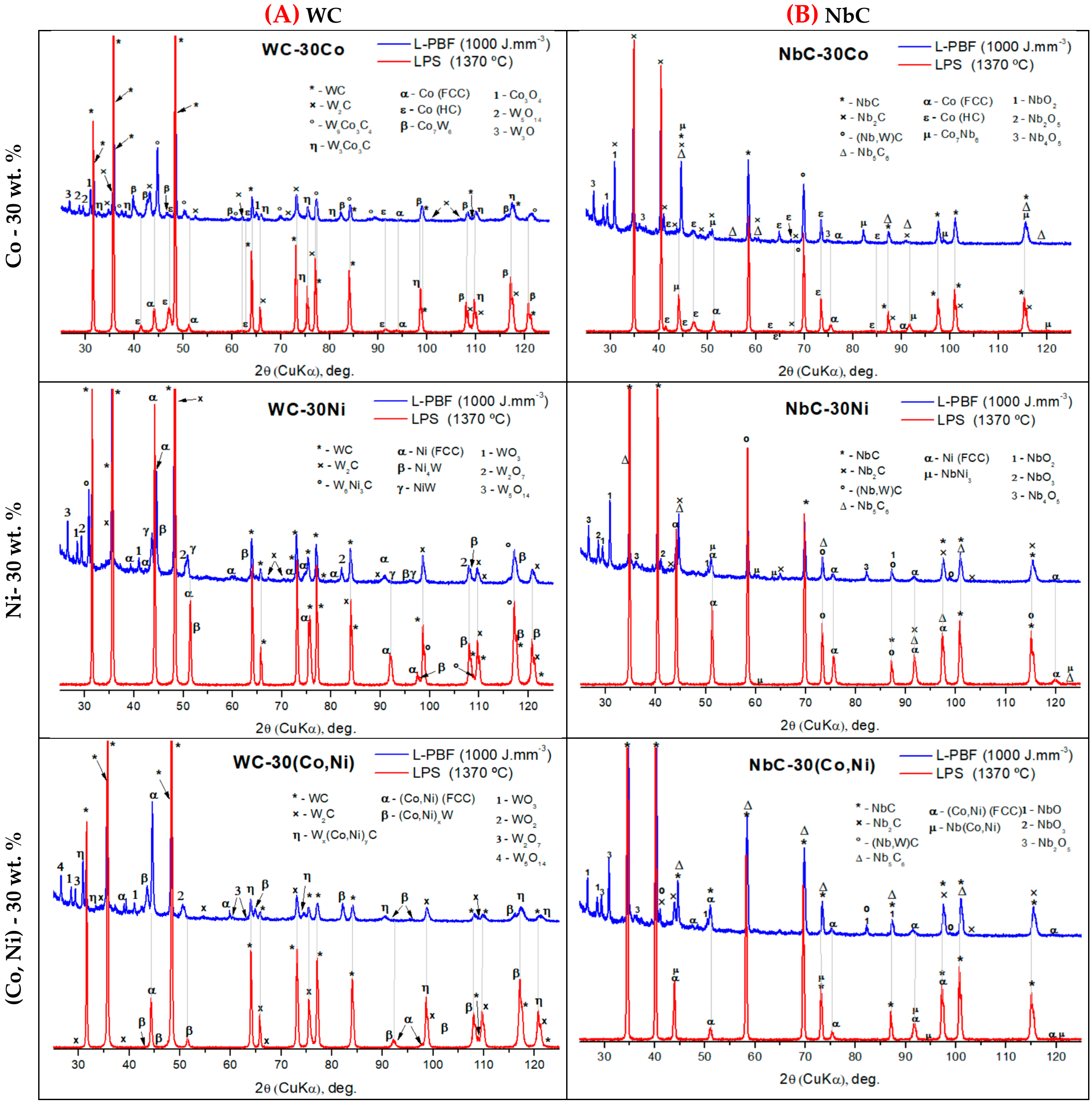

Figure 24. XRD patterns of samples XIII with parameters: P_L = 125 W, v_S = 25 $mm.s^{-1}$ and VED = 1000 $J.mm^{-3}$ (~300 ppm of O_2) and sample of the conventional LPS route: 1370 °C (<50 ppm of O_2), 30 min and 50 MPa for comparison purposes; (**A**) WC-based alloys; and (**B**) NbC-based alloys.

For the WC-30Ni alloy, with a considerable carbon loss, the dissolution of W is most likely, and three phases can form during solidification, with the first phase being the NiW compound, with a composition of 75.8 wt.% of W. Second, in inhomogeneous regions, with 44 wt.% of W, the Ni_4W compound and the NiW_2 compound (86.3 wt.% W) can form, whose formation is susceptible to the presence of oxygen in the system [59], forming the oxides WO_3 (COD ID 1521534), $WO_{2.72}$ (COD ID 1538315), W_2O_7 (COD ID 9014038), and W_5O_{14} (COD ID 1527783). For the WC-30Co and WC-30(Co, Ni) alloys, the oxides formed were Co_3O_4 (COD ID 5910031), $Co_{2.72}O_4$ (COD ID 1528446), CoO (COD ID 1541662), and WO_3 (COD ID 1521534). The WC-30(Co, Ni) alloy behaves similarly to the WC-30Ni alloy, creating the same compounds and oxides. Alternative compositions for W- and Ni-based refractory alloys can be efficiently designed for specific applications, provided the embrittlement of the intermetallic precipitations for alloys with Ni-rich binders is avoided, as they form the Ni_4W (COD ID 1523560), $Ni_{0.85}W_{0.15}$ (COD ID 1523162), and $Ni_{0.92}W_{0.08}$ (COD ID 1523346) compounds for slow and fast cooling. These phases can be eliminated by a post-intermediate heat treatment [60].

For NbC-based cermet alloys, the addition of 3 wt.% of WC was observed to dissolve in the metallic binder during L-PBF sintering, since no significant peaks were observed in the XRD for WC. Nonetheless, some W combined with Nb was confirmed, forming the (Nb, W) C phase, showing that WC can be dissolved in both phases: solid–solid and solid–liquid [13]. The purpose of adding WC to NbC-based alloys was to prevent abnormal grain growth and contribute to the hardening of the binder phase, which consequently increases the hardness of NbC-based alloys, matching the hardness of conventional WC-based alloys obtained via LPS sintering [11,16]. XRD diffractometry also showed that NbC (COD ID 9008682) transformed into Nb_2C (COD ID 1540810), presenting very different crystalline structures, FCC and HC, respectively [42]. Nb_6C_5 (COD ID 1536531), another intermetallic compound that appeared during melting and precipitation, was also detected, which is undesirable, as it increases the brittleness and decreases the mechanical strength of cemented carbide alloys. In addition, oxides such as NbO_2 (COD ID 9009093), NbO_3 (COD ID 9015165), and Nb_4O_5 (COD ID 1534619) were present in the phase analysis.

Finally, the resulting structures of the WC- and NbC-based alloys via L-PBF were heterogeneous for the different VED levels compared to the sintering technique via LPS. Further scientific research is necessary regarding direct sintering techniques via L-PBF for cemented carbide alloys with alternative binder phases, evaluating different factors, such as materials (chemical composition, particle size, and shape), sintering conditions and parameters ($P_L \times v_S$), which are the main obstacles. The undesirable effects include porosity, carbon loss, heterogeneous structure, abnormal grain growth, formation of intermetallic phases or compounds, microcracks, and good bonding of particles and deposition layers. These problems are still to be better understood with more advanced studies [43,61].

4. Conclusions

The best powder flow conditions are observed in samples containing only Co, close to the WC-30Co samples, which have good flowability, whereas the NbC-30Ni samples have poor flowability. The porosity of the NbC-30Co mixture is more significant, requiring a better compaction technique in the powder bed to produce a flawless part. The packing of the mixtures for the NbC-based alloys indicated higher levels of cohesion than the WC-based alloys due to the increased particle size and density. The WC-30Ni alloy powder mixture with the presence of larger Ni particulates (~10 µm) had more efficient particle packing when compared to the NbC-based alloys (<1 µm) with Co, since coarser and denser particles tend to flow more freely in the powder bed and can therefore slide over each other to form a more compacted powder bed. The NbC-based alloy samples presented critical porosities after sintering via L-PBF when compared to the WC-based alloys. The WC samples containing Ni presented lower porosity, producing a particle bed with fewer voids during compaction. The strategies for different VED levels ($P_L \times V_S$) created in this work provide the laser operating conditions for validating the critical functions of a prototype (reduced scale of large parts) in a relevant environment. The WC-based alloys performed better than the NbC-based alloys, which need improvements. The recommended conditions to avoid undesirable effects (cracks, carbon and binder phase losses) for WC-based and NbC-based alloys with high binder phase content (30 wt.%) are VEDs from 250 to 330 J.mm^{-3}. VEDs above 300 J.mm^{-3} easily aggravated the formation of cracks and fissures. For VEDs below 417 J.mm^{-3}, they contributed to the formation of macroporosities, leading to a poor relative density for the specimens.

Direct sintering via L-PBF generated distinct regions in the microstructures: one region is similar to the alloys processed via LPS with primary WC carbides, the second region is composed of W_2C (decomposition) phases and eta-η (ternary) phases, and the third region with dendrites. For the NbC-based alloys, Nb_2C, Nb_5C_6 and ternary phases were formed. Increasing the laser power contributed to the carbon loss, evaporation of the binder phase, formation of metal oxides and increased residual thermal stresses, resulting in microcracks. Increasing the scanning speed results in increased apparent porosity. Increasing the laser power increases the temperature over a wide range, leading to the formation and enlargement of the WC decomposition region. The WC-30Co alloy samples presented the highest number of cracks for VEDs above 333 J.mm^{-3} due to the thermal residual stresses; the allotropic transformation of Co contributed to this effect.

The WC- and NbC-based alloys with Ni presented the lowest values of thermal residual stress, below—50 MPa (compressive stress). Regarding the microstructures of the WC-based alloys, they presented abnormal grain growth and decomposition, loss of carbon and formation of eta-n phases, ternary phases and intermetallic compounds. In addition, there was the presence of small amounts of oxides. The interdendritic and dendritic regions were evidenced for WC-based alloys with Co, Ni, and their combination (Co, Ni) binder phases for alloys sintered above VED = 300 J.mm^{-3}. For WC-30Co, the binder phase comprises primary dendrites (hypo eutectic structure), and for the WC-30Ni alloy, interdendritic eutectics.

The microhardness of the WC-30Ni and WC-30(Co, Ni) alloys, via L-PBF, for all the sintering parameters ($P_L \times v_S$), presented values close to the reference values of the traditional WC-30Co alloy HV1 = 800 to HV1 = 1000. For the WC- and NbC-based alloys combined with Co, some samples resulted in values higher than HV1 > 1000 due to the hardening of the binder phase, evaporation of the binder phase, presence of intermetallic phases, eta-n phase, metal oxides, etc. The WC- and NbC-based alloys with Ni presented lower thermal residual stress values for energies below VED = 417 J.mm^{-3}, when compared to the Co-based alloys, which were the samples with the highest number of cracks due to allotropic transformation.

5. Future Directions

Demonstrating the critical functions of a prototype in a relevant environment, we are considering the following suggestions to proceed with this work: corrections of WC- and NbC-based mixtures with the addition of free carbon (carbon black) or at the request of carbide manufacturers (raw material), with combined carbon close to the levels of 10 wt.% C for NbC and 6.1 wt.% C for WC, to avoid the emergence of eta-η phases and other compounds. Furthermore, grain growth inhibitors will be added to WC and NbC. Improvements and new studies on the rheology of NbC cermet-based mixtures. Studying the variation in the compaction pressure of WC- and NbC-based mixtures in the powder bed, with the metal roller rotating clockwise and counterclockwise. The L-PBF parameters for WC- and NbC-based carbide alloys with high binder phase content, as defined in this study, can potentially be applied (with the pneumatic vibratory device) to the manufacturing of pilot-scale parts for complex shapes with high relative density and without microcracks for energies below VED = 300 J.mm^{-3}. Comparing the direct sintering techniques (L-PBF) with a dynamic flow atmosphere (argon or nitrogen) with the vacuum chamber (2×10^{-5} mbar in terms of carbon loss, wt.% C) and performing heat treatment via vacuum sintering to eliminate possible cracks and dendrites, if necessary.

Author Contributions: F.M.: writing—original draft, resources, conceptualization, data curation, formal analysis, investigation, methodology, visualization; dos Santos, M.O.d.S.: writing—review and editing, validation and methodology; R.C.: writing—review and editing, validation and methodology; Pereira, N.M.G.P.: validation and methodology; D.R.: conceptualization, funding acquisition, project administration, resources, validation and supervision; S.R.J.: funding acquisition, project administration, resources, validation, supervision, conceptualization, writing—review and editing; F.d.S.O.: conceptualization, validation, methodology and writing—review and editing; M.V.M.: validation and writing—review and editing; R.S.C.: validation and writing—review and editing; R.R.d.O.: validation and methodology; L.G.M.: validation and methodology; and G.F.B.: conceptualization, validation and supervision. All authors have read and agreed to the published version of the manuscript.

Funding: This study was financed, in part, by the São Paulo Research Foundation (FAPESP), Brasil. Research Grant—Innovative Research in Small Businesses—PIPE, Process Number #2022/06201-7.

Data Availability Statement: Data will be made available on request.

Acknowledgments: The authors thank the University Center FEI, Mauá Institute of Technology, the Institute of Energy and Nuclear Research (IPEN), and the company Brats Filters and Metal Powders for carrying out the experimental tests. Furthermore, the authors acknowledge the financial support from the São Paulo Research Foundation (FAPESP), Brazil.

Conflicts of Interest: The authors declare that they have no known competing financial interests or personal relationships that could have appeared to influence the work reported in this paper. The funders had no role in the study design, in the collection, analyses, or interpretation of data, in the writing of the manuscript, or in the decision to publish the results.

References

1. Roulon, Z.; Missiaen, J.-M.; Lay, S. Carbide grain growth in cemented carbides sintered with alternative binders. *Int. J. Refract. Met. Hard Mater.* **2019**, *86*, 105088. [CrossRef]
2. Acchar, W.; Zollfrankb, C.; Greilb, P. Microstructure and Mechanical Properties of WC-Co Reinforced with NbC. *Mater. Res.* **2004**, *7*, 445–450. [CrossRef]
3. Jucan, O.-D.; Gadalean, R.-V.; Chicina¸S, H.-F.; Bâlc, N.; Popa, C.-O. The Assessment of the Transversal Rupture Strength (TRS) and Hardness of WC-Co Specimens Made via Additive Manufacturing and Sinter-HIP. *Metals* **2023**, *13*, 1051. [CrossRef]
4. Miranda, F.; Fernandes, L.J.; Batalha, M.H.; Rodrigues, D.; Stoeterau, R.L.; Batalha, G.F. Critical raw materials in cutting tools for machining applications—A review. *Braz. J. Dev.* **2021**, *7*, 49513–49537. [CrossRef]
5. Miranda, F.; Stoeterau, R.L.; Batalha, G.F. Occupational Risks in the Manufacture of Products Heavy Alloy and Hardmetals Cutting Tools in the Mechanical Industry. *Glob. J. Med. Res. K Interdiscip.* **2021**, *21*, 29–51. [CrossRef]
6. Akira, M.; Suganuma, N. Hard metal lung disease. *Health Sci. Rev.* **2024**, *11*, 10016. [CrossRef]
7. McCullough, E.; Nassar, N.T. Assessment of critical minerals: Updated application of an early-warning screening methodology. *Miner. Econ.* **2017**, *30*, 257–272. [CrossRef]
8. Labonne, M.; Missiaen, J.-M.; Lay, S.; García, N.; Lavigne, O. Sintering behavior and microstructural evolution of NbC-Ni cemented carbides with Mo2C additions. *Int. J. Refract. Met. Hard Mater.* **2020**, *92*, 105295. [CrossRef]
9. Alam, M.E.; Wang, J.; Henager, C.H., Jr.; Setyawan, W.; Odette, G.R. The effect of hot rolling on the strength and fracture toughness of 90W–7Ni3Fe tungsten heavy metal alloys. *Mater. Sci. Eng. A.* **2021**, *824*, 141738. [CrossRef]
10. Correa, E.O.; Santos, J.N.; Klein, A.N. Microstructure and mechanical properties of WC Ni–Si-based cemented carbides developed by powder metallurgy. *Int. J. Refract. Met. Hard Mater.* **2010**, *28*, 572–575. [CrossRef]
11. Fernandes, L.J.; Stoeterau, R.L.; Batalha, G.F.; Rodrigues, D.; Borrile, A.V. Wear analysis of NbC-Ni cemented carbides for cutting tools. *Adv. Mater. Process. Technol.* **2022**, *8*, 305–321. [CrossRef]
12. Franco, E.; Costa, C.; Tsipas, S.; Gordo, E. Cermets based on FeAl–NbC from composite powders: Design of composition and processing. *Int. J. Refract. Met. Hard Mater.* **2015**, *48*, 324–332. [CrossRef]
13. Huang, S.G.; Liu, R.L.; Li, L.; Van Der Biest, O.; Vleugels, J. NbC as grain growth inhibitor and carbide in WC–Co hardmetals. *Int. J. Refract. Met. Hard Mater.* **2008**, *26*, 389–395. [CrossRef]
14. Huang, S.G.; Li, L.; Van Der Biest, O.; Vleugels, J. Influence of WC addition on the microstructure and mechanical properties of NbC-Co cermets. *J. Alloys Compd.* **2007**, *430*, 158–164. [CrossRef]
15. Cuppari, M.; Santos, S. Physical Properties of the NbC Carbide. *Metals* **2016**, *6*, 250. [CrossRef]
16. Rodrigues, D.; Cannizza, E. The use of NbC20Ni Hard materials for hot rolling applications. In Proceedings of the 19th Plansee Seminar 2017, Reutte, Austria, 29 May–2 June 2017; Volume 3.
17. Li, J.; Wei, Z.; Zhou, B.; Wu, Y.; Chen, S.-G.; Sun, Z. Densification, Microstructure and Properties of 90W-7Ni-3Fe Fabricated by Selective Laser Melting. *Metals* **2019**, *9*, 884. [CrossRef]

18. Sidambe, A.; Tian, Y.; Prangnell, P.; Fox, P. Effect of processing parameters on the densification, microstructure, and crystallographic texture during the laser powder bed fusion of pure tungsten. *Int. J. Refract. Met. Hard Mater.* **2018**, *78*, 254–263. [CrossRef]
19. Wang, D.; Yu, C.; Zhou, X.; Ma, J.; Liu, W.; Shen, Z. Dense Pure Tungsten Fabricated by Selective Laser Melting. *Appl. Sci.* **2017**, *7*, 430. [CrossRef]
20. Campanelli, S.; Contuzzi, N.; Posa, P.; Angelastro, A. Printability and Microstructure of Selective Laser Melting of WC/Co/Cr Powder. *Materials* **2019**, *12*, 2397. [CrossRef]
21. García, J.; Collado Ciprés, V.; Blomqvist, A.; Kaplan, B. Cemented carbide microstructures: A review. *Int. J. Refract. Met. Hard Mater.* **2018**, *80*, 40–68. [CrossRef]
22. Miranda, F.; Maiolini, A.; Dos Santos, M.O.; Rodrigues, D.; Janasi, S.R.; Batalha, G.F. Towards the flowability and spreadability of cemented carbides and cermet powders for Additive Manufacturing: Experimental and numerical approach—Part 1. In Proceedings of the 27th International Congress of Mechanical Engineering, Rio de Janeiro, Brazil, 4–8 December 2023. [CrossRef]
23. Budding, A.; Vaneker, T. New Strategies for Powder Compaction in Powder-based Rapid Prototyping Techniques. *Procedia CIRP* **2013**, *6*, 528–533. [CrossRef]
24. Freeman, T.; Bey, H.; Hanish, M.; Brockbank, K.; Armstrong, B. The influence of roller compaction processing variables on the rheological properties of granules. *Asian J. Pharm. Sci.* **2016**, *11*, 516–527. [CrossRef]
25. Santos, L.C.; Condotta, R.; Ferreira, M.C. Flow properties of coarse and fine sugar powders. *J. Food Process Eng.* **2017**, *41*, e12648. [CrossRef]
26. Gururajan, B.; Seville, J.P.K.; Adams, M.; Greenwood, R.; Fitzpatrick, S. Roll compaction of a pharmaceutical excipient: Experimental validation of rolling theory for granular solids. *Chem. Eng. Sci.* **2005**, *60*, 3891–3897. [CrossRef]
27. Aramian, A.; Razavi, M.; Sadeghian, Z.; Berto, F. A Review of Additive Manufacturing of Cermets. *Addit. Manuf.* **2020**, *33*, 101130. [CrossRef]
28. Uhlmann, E.; Bergmann, A.; Gridin, W. Investigation on Additive Manufacturing of Tungsten Carbide-Cobalt by Selective Laser Melting. *Procedia CIRP* **2015**, *35*, 8–15. [CrossRef]
29. Zegzulka, J.; Gelnar, D.; Jezerská, L.; Prokes, R.; Rozbroj, J. Characterization and flowability methods for metal powders. *Sci. Rep.* **2020**, *10*, 21004. [CrossRef]
30. Freeman, R. Measuring the flow properties of consolidated, conditioned and aerated powders—A comparative study using a powder rheometer and a rotational shear cell. *Powder Technol.* **2007**, *174*, 25–33. [CrossRef]
31. Debroy, T.; Wei, H.; Zuback, J.; Mukherjee, T.; Elmer, J.; Milewski, J.O.; Beese, A.; Wilson-Heid, A.; De, A.; Zhang, W. Additive manufacturing of metallic components—Process, structure, and properties. *Prog. Mater. Sci.* **2018**, *92*, 112–224. [CrossRef]
32. Marchetti, L.; Hulme-Smith, C. Flowability of steel and tool steel powders: A comparison between testing methods. *Powder Technol.* **2021**, *384*, 402–413. [CrossRef]
33. Pal, S.; Drstvensek, I.; Brajlih, T. Physical behaviors of materials in selective laser melting process. In *DAAAM International Scientific Book 2018*; DAAAM International Vienna: Vienna, Austria, 2018; pp. 239–256. [CrossRef]
34. *ASTM Standard B276-21*; Evaluation of Apparent Porosity in Cemented Carbides. ASTM International: West Conshohocken, PA, USA, 2021. Available online: https://www.astm.org/b0276-21.html (accessed on 17 March 2023).
35. *ASTM Standard B657-92*; Standard Test Method for Metallographic Determination of Microstructure in Cemented Tungsten Carbides. ASTM International: West Conshohocken, PA, USA, 2000. Available online: https://www.astm.org/b0657-92r00.html (accessed on 16 August 2017).
36. Miranda, F.; Dos Santos, M.O.; Rodrigues, D.; Batalha, G.F.; Janasi, S.R.; Ortega, F.S. WC Cemented Carbides: Microstructural aspects comparing L-PBF Additive Manufacture and convencional LPS. In Proceedings of the Euro Powder Metallurgy 2023 Congress & Exhibition, Lisbon, Portugal, 1–4 October 2023. [CrossRef]
37. Miranda, F.; Santos, M.O.; Coelho, R.S.; Rodrigues, D.; Batalha, G.F. NbC-based Cermet production comparison: L-PBF Additive Manufacturing versus conventional LPS powder metallurgy. *Mater. Tehnol.* **2023**, *57*, 129–137. [CrossRef]
38. Xing, M.; Wang, H.; Zhao, Z.; Lu, H.; Liu, C.; Lin, L.; Wang, M.; Song, X. Additive manufacturing of cemented carbide inserts with high mechanical performance. *Mater. Sci. Eng. A* **2022**, *861*, 144350. [CrossRef]
39. Schwanekamp, T.; Marginean, G.; Reuber, M.; Ostendorf, A. Impact of cobalt content and grain growth inhibitors in laser-based powder bed fusion of WC-Co. *Int. J. Refrac. Met. Hard Mat.* **2022**, *105*, 105814. [CrossRef]
40. Lee, S.W.; Kim, Y.W.; Jang, K.M.; Lee, J.W.; Park, M.-S.; Koo, H.Y.; Ha, G.-H.; Kang, Y.C. Phase control of WC–Co hardmetal using additive manufacturing technologies. *Powder Metall.* **2022**, *65*, 13–21. [CrossRef]
41. Vreeswijk, M.; Kot, A.; Giuliani, F.; Humphry-Baker, S. Abnormal WC crystal growth from liquid Co flux occurs via eta phase decomposition. *Int. J. Refract. Met. Hard Mater.* **2021**, *99*, 105589. [CrossRef]
42. Fernandes, C.M.; Senos, A.M.R. Cemented carbide phase diagrams: A review. *Int. J. Refract. Met. Hard Mater.* **2011**, *29*, 405–418. [CrossRef]
43. Serkhane-Ouabadi, N.; Benalia-Baguenane, G.; Nechiche, M.; Azemu, S. Influence of the liquid phase and the carbon on the reactive sintering in mixtures W-Ni-C. *U.P.B. Sci. Bull.* **2022**, *84*, 109–122.
44. Jose, S.A.; John, M.; Menezes, P.L. Cermet Systems: Synthesis, Properties, and Applications. *Ceramics* **2022**, *5*, 210–236. [CrossRef]
45. Straumal, B.B.; Konyashin, I. Faceting/Roughening of WC/Binder Interfaces in Cemented Carbides: A Review. *Materials* **2023**, *16*, 3696. [CrossRef]

46. Woydt, M.; Huang, S.; Vleugels, J.; Mohrbacher, H.; Cannizza, E. Potentials of niobium carbide (NbC) as cutting tools and for wear protection. *Int. J. Refract. Met. Hard Mater.* **2018**, *72*, 380–387. [CrossRef]
47. Huang, S.G.; De Baets, P.; Sukumaran, J.; Mohrbacher, H.; Woydt, M.; Vleugels, J. Effect of Carbon Content on the Microstructure and Mechanical Properties of NbC-Ni Based Cermets. *Metals* **2018**, *8*, 178. [CrossRef]
48. Lv, N.; Yue, H.; Guo, C.; Dai, W.; Zhang, J.; Li, Q.; Zhao, G.; Hao, G. A comparative investigation on the effects of reinforcement phase addition methods on laser melting deposited WC/Co coatings. *J. Manuf. Process.* **2024**, *129*, 134–146. [CrossRef]
49. Sarin, V.; Mari, D.; Llanes, L.; Nebel, C.E. *Comprehensive Hard Materials*; Elsevier: Amsterdam, The Netherlands, 2014; Volume I, p. 700.
50. *ISO Standard 3878-1983(E)*; Hardmetals—Vickers Hardness Test. ISO International Standard: Geneva, Switzerland, 1983. Available online: https://www.iso.org/standard/9484.html (accessed on 8 October 2024).
51. Chen, C.; Huang, B.; Liu, Z.; Li, Y.; Zou, D.; Liu, T.; Chang, Y.; Chen, L. Additive manufacturing of WC-Co cemented carbides: Process, microstructure, and mechanical properties. *Addit. Manuf.* **2023**, *63*, 103410. [CrossRef]
52. Khmyrov, R.S.; Shevchukov, A.P.; Gusarov, A.V.; Tarasova, T.V. Phase composition and microstructure of WC–Co alloys obtained by selective laser melting. *Mech. Ind.* **2017**, *18*, 714. [CrossRef]
53. Zhang, F.L.; Wang, C.Y.; Zhu, M. Nanostructured WC/Co composite powder prepared by high energy ball milling. *Scripta Mat.* **2003**, *49*, 1123–1128. [CrossRef]
54. Balbino, N.A.N.; Corrêa, E.O.; Huanca, D.R.; de Freitas Matos, F.A.; de Carvalho Valeriano, L. Comparative Study of Corrosion Behaviors of WC-NiMo and WC-Co Cemented Carbides. *Materials* **2023**, *16*, 4480. [CrossRef]
55. Li, X.; Zhang, X.; Zhang, J.; Zhang, Q.; Ji, V.; Liu, J. Effect of Mo and C Additions on Eta Phase Evolution of WC-13Co Cemented Carbides. *Coatings* **2022**, *12*, 1993. [CrossRef]
56. Chicinas, H.F.; Marinca, T.F.; Götze, P.; Eckert, A.; Popa, C.O. Influence of aqueous milling duration on the sintered WC–10Co hard metal powders. *J. Mater. Sci.* **2018**, *53*, 2901–2910. [CrossRef]
57. Tran, S. Microstructure Investigations of WC-Co Cemented Carbide Containing η-Phase and Cr. Master's Thesis, Uppsala University, Uppsala, Sweden, 8 August 2018; p. 51.
58. Upadhyaya, G.S. *Cemented Tungsten Carbides: Production, Properties, and Testing*; Noyes Publications: Norwich, NY, USA, 1998; p. 27, ISBN 0-8155-1417-4. Available online: https://books.google.com.br/books?id=9UVcIa8M4V8C&printsec=frontcover&hl=pt-BR&source=gbs_ge_summary_r&cad=0#v=onepage&q&f=false (accessed on 15 October 2024).
59. Enneti, R.; Morgan, R.; Wolfe, T.; Harooni, A.; Volk, S. Direct Metal Laser Sintering (DMLS) of Tungsten Powders. *Int. J. Powder Metall.* **2017**, *53*, 23–31.
60. Funch, C.V.; Proust, G. Laser-based additive manufacturing of refractory metals and their alloys: A review. *Addit. Manuf.* **2024**, *94*, 104464. [CrossRef]
61. Chhabra, D. Comparison and analysis of different 3d printing techniques. *Int. J. Latest Trends Eng. Technol.* **2017**, *8*, 264–272. [CrossRef]